npj Flexible Electronics

https://doi.org/10.1038/s41528-026-00618-5

Article in Press

System-level transient simulation of bioresorbable and flexible electronic circuits

Received: 9 March 2026

Accepted: 4 July 2026

Published online: 11 July 2026

Cite this article as: Liu, P., Garmroudi, A., Li, Z. *et al.* System-level transient simulation of bioresorbable and flexible electronic circuits. *npj Flex Electron* (2026). https://doi.org/10.1038/s41528-026-00618-5

Pei Liu, Ali Garmroudi, Zhengwei Li & Raudel Avila

System-level Transient Simulation of Bioresorbable and Flexible Electronic Circuits.

Authors

Pei Liu[1], Ali Garmroudi[2], Zhengwei Li[2,3], and Raudel Avila[1,4,5,6,7,*]

Affiliations

[1]Department of Mechanical Engineering, Rice University, Houston, Texas, 77005
[2]Department of Biomedical Engineering, University of Houston, Houston, Texas, 77204
[3]Department of Biomedical Sciences, University of Houston, Houston, Texas, 77204
[4]Rice Advanced Materials Institute, Rice University, Houston, Texas, 77005
[5]Rice Neuroengineering Initiative, Rice University, Houston, Texas, 77005
[6]Digital Health Institute, Rice University, Houston, Texas, 77005
[7]Ken Kennedy Institute, Rice University, Houston, Texas, 77005

*Corresponding author: Raudel Avila
Email: ra88@rice.edu

Keywords
Transient Electronics
Computational Modeling
Bioresorbable Electronics
Mechanics
Electromagnetics

Abstract

Bioresorbable electronics promise safe, time-limited operation in the body, eliminating the risks of secondary surgery. Their clinical translation, however, requires quantitative models that link degradation kinetics to system-level electromechanical and electromagnetic performance over clinically relevant timescales, enabling reliable function in implants for electrotherapy, physiological monitoring, neural interfaces, and drug delivery. We introduce a computational framework that uniquely couples diffusion–reaction degradation with mechanical and electrical response, enabling quantitative prediction of transient performance in representative bioresorbable devices. Specifically, we benchmark the framework against seminal dissolution experiments on silicon nanomembranes, biomimetic bladders, and established analytical theories and scaling laws, reproducing experimental dissolution kinetics within ~1.6% error. We demonstrate system-level transient response in radio-frequency resonators, pressure sensors, strain sensors, and general classes of stretchable electronic systems. Beyond dissolution, the framework models functional metrics, including increases in electrical resistance, shifts in resonant frequency, and partial/complete circuit fracture, as bioresorbable devices degrade, providing a capability that bridges in silico prediction with *in vitro* characterization and ultimately *in vivo* performance.

MAIN TEXT

Introduction

Bioresorbable electronic systems represent a distinct class of implantable technologies that operate temporarily in the body and then disappear through biologically driven chemical dissolution (1, 2). Their transient nature, enabled by carefully selected bioresorbable materials (3–6), eliminates the need for surgical extraction and reduces long-term post-operative risks associated with chronic implants. Recent demonstrations of bioresorbable pacemakers (7), neural stimulators (8–13), drug delivery platforms (14–20), and physiological sensors (21–27) highlight the clinical promise of these systems. Realizing this translational promise critically depends on a quantitative understanding of how material degradation and mechanical deformation coevolve to determine functional lifetime under physiological conditions.

The degradation of bioresorbable electronics depends on a coupling of diffusion, reaction, and stress-driven processes (1, 28). Hydrolysis and oxidation reduce elastic modulus and carrier mobility, while geometry changes from deformation, swelling, or mass loss modify current density, strain localization, and fracture onset (29–31). Conversely, tensile and bending stress introduce stress-assisted diffusion (32–34) and promote interfacial delamination, thereby accelerating local reaction kinetics. Bioresorbable electronic systems vary widely in their constituent materials, structural layouts, and intended functions, from active stimulation and drug-delivery platforms to passive sensing technologies. These differences lead to different deformation states during operation, which in turn influence the extent to which mechanical loading modifies degradation. As a result, the appropriate description of degradation may range from one-way coupling, where mechanics has a negligible influence on resorption, to two-way coupling, where stress fields significantly modify degradation kinetics. **Table 1** compares representative bioresorbable electronic systems and classifies them into one-way or two-way coupling regimes based on the strain in the conductive element. Definitions of all material nomenclature appear in the Supplementary Information.

Existing bioresorbable degradation models are either one-dimensional reactive-diffusion approximations or phenomenological damage-based models. Analytical models of reactive-diffusion for transient electronics (28) and kinetic formulations of hydrolytic and oxidative degradation in biodegradable polymers (44) provide first-order lifetime estimates based on resistive or mass-loss changes in electronic materials such as monocrystalline silicon, magnesium, and polymer encapsulations, including natural materials (e.g., silk, gelatin, candelilla wax) and synthetic systems such as polylactic acid (PLA) and polyanhydrides as well as conductive pastes and organic electronic materials. However, their one-dimensional formulations neglect the spatially heterogeneous dissolution chemistry, swelling, and multiaxial deformation that govern degradation and failure in multilayer, stretchable bioresorbable electronic systems (6, 35, 36). Consequently, the current understanding of degradation and lifetime in bioresorbable systems is primarily grounded in experimental observation of system-level degradation and simplified electrode benchtop experiments rather than in predictive, physics-based modeling. Damage-based models have primarily focused on implantable stents, emphasizing structural performance during progressive material loss (45, 46). These frameworks incorporate mechanisms such as pitting (47), corrosion-induced damage (48), and surface recession (49) to predict mass loss and structural failure. In most formulations, however, degradation kinetics are imposed through prescribed material rates or empirical fitting (49, 50) rather than physically closed descriptions of material resorption and are often implemented using mesh-dependent element-deletion schemes. As a result, their applicability is largely restricted to simple geometries and loading conditions, limiting their predictive utility for bioelectronic systems (51). **Supplementary Table 1** compares the present framework with prior models for bioresorbable electronics. The framework uniquely combines spatially resolved degradation with

prediction of system-level electrical, mechanical, and electromagnetic responses throughout the resorption process.

Prior computational studies for bioresorbable electronics have primarily examined either the diffusion-controlled dissolution of device materials (28, 44) or the mechanical response of horseshoe-shaped serpentine interconnects (52) in isolation, overlooking the feedback between chemical degradation and mechanical stress that ultimately governs system-level performance. Addressing these coupled processes requires a modeling framework that self-consistently links diffusion–reaction degradation with evolving mechanical fields to quantitatively predict how material resorption modifies stiffness, stress distribution, and electrical pathways in realistic, clinically relevant device geometries.

Here, we report a computational framework that unifies diffusion–reaction degradation kinetics with evolving mechanical and electrical responses to establish quantitative design rules for bioresorbable electronic systems. The density-based finite element model captures the temporal evolution of material resorption by solving diffusion–reaction equations and linking them to elasticity, thereby updating geometry, stiffness, and stress distributions as degradation proceeds. Validation against published dissolution data for silicon nanomembranes (53) and analytical scaling laws (28) confirms its accuracy in reproducing both dissolution rate and spatial progression of material loss. Further experimental demonstrations using a soft biomimetic bladder integrated with a bioresorbable pressure sensor demonstrate the ability of the framework to predict system-level functional responses during resorption. The framework serves as a predictive tool for system-level performance, quantified through representative examples that include electrode arrays, radio-frequency resonators, pressure and strain sensors, and stretchable interconnects. Multiphysics simulations across these bioelectronic device platforms reveal the mechanistic pathways through which degradation modifies electrical resistance, resonant frequency, and structural integrity, establishing the basis for system-level design of bioresorbable devices with programmable lifetime, stability, and functionality.

Results

Modeling Schemes for Transient Degradation

Fig. 1 presents experimental and numerical results that illustrate representative modes of transient degradation in magnesium thin films. Cyclic mechanical deformation (***F***) in soft biological tissue, such as the epicardium (**Fig. 1A**), modifies diffusion processes (***D***) and accelerates or delays degradation through surface- and bulk-degradation pathways (**Fig. 1B**). Materials with diffusion rates slower than their reaction rates, such as silicon, silk, and magnesium oxide (MgO), undergo surface-limited degradation dominated by interfacial reactions(54, 55). In contrast, (Mg) exhibits bulk degradation, where fluid permeates the solid and drives volumetric reactions that progressively reduce the thickness and microstructural density (28, 56, 57). To capture both degradation modes within a unified formulation, we develop a density-based finite element framework that represents degradation through the element-wise solid density (ρ_e) and water concentration (w_e) as:

$$w_e = (1 - \rho_e)H(\epsilon - \rho_e) \tag{1}$$

where ρ_e denotes the element-wise solid density, and $H(\epsilon - \rho_e)$ is the Heaviside function with a small threshold ϵ, used to represent the local remaining material fraction in the element during degradation. For surface limited degradation, $\rho_e > \epsilon$ yields $H(\epsilon - \rho_e) = 0$, preventing fluid diffusion until the solid density approaches zero. For bulk degradation, ρ_e decreases continuously and satisfies $\rho_e \leq \epsilon$, enabling fluids to permeate the element and drive volumetric dissolution. **Fig. 1C** illustrates the degradation boundary conditions and the application of a density filter to each element e over its local neighborhood Ω_e within a fixed radius r_{filter}. The filter, adapted from density-based topology optimization (58, 59), incorporates the influence of neighboring elements w_j and defines an effective element concentration $\widetilde{w}_e$ as

$$\widetilde{w}_e = \frac{\sum_{j\epsilon\Omega_e} w_j d(x_j - x_e)}{\sum_{j\epsilon\Omega_e} d(x_j - x_e)} \tag{2}$$

where $d(x_j - x_e)$ is a distance-based weight function and x_j denotes the centroid of the element j. This formulation smooths local concentration fields and provides a consistent basis for evaluating concentration gradients during degradation. System-level degradation in bioresorbable electronics is inherently three-dimensional. Because the in-plane dimensions of these circuits (cm-scale) are much larger than their thickness (μm-scale), we separate degradation into in-plane and out-of-plane components. We express the temporal evolution of the element-wise density as

$$\frac{d\rho_e}{dt} = \begin{cases} \mathrm{C}_\perp + \mathrm{C}_\parallel \Delta w_e & \text{surface} \\ \mathrm{C}_\perp \rho_e + \mathrm{C}_\parallel \Delta w_e & \text{bulk} \end{cases} \tag{3}$$

where $\mathrm{C}_\perp$ and $\mathrm{C}_\parallel$ are the out-of-plane and in-plane degradation coefficients (units of 1/s), respectively, and $\Delta w_e = \widetilde{w}_e - w_e$ represents the local concentration difference between element e and its neighbors. In bulk-degradation, multiplicative dependence on ρ_e introduces a nonlinear saturation behavior as the material volume vanishes. The full numerical algorithm is described in **Supplementary Note 1** and **Supplementary Fig. 1**. The equivalence between the density-filter formulation and reaction–diffusion physics in Eq. (3) is detailed in **Supplementary Note 2**, with corresponding validation and verification results on a 200×200 mesh for anisotropic and periodic density fields shown in **Supplementary Fig. 2**.

A time step of $\Delta t = 0.005$ satisfies the CFL stability condition and yields a smooth, converged density field (**Supplementary Fig. 3**).

Surface-limited degradation in silicon nanomembranes (Si NMs), as reported by Hwang et al. (2012 (53) and 2014 (3)), is used to validate the model. A 3 μm × 3 μm × 70 nm Si NM is simulated at four representative pH values (6, 7, 8, and 12), with the physiological temperature of 37 °C in accelerating dissolution from months to hours. **Fig. 1D** shows that the model reproduces the experimentally observed linear thickness loss, with a maximum error of 7.5% and a mean error across all pH values below 2%. **Fig. 1E** illustrates the predicted 3D dissolution geometry of a 70-nm-thick Si NM at pH 7.4. Atomic force microscopy measurements from Hwang et al. (2012) (53) in **Supplementary Fig. 4** quantify the thickness evolution of the Si NMs over a 12-day dissolution period in phosphate-buffered saline (PBS, pH 7.4). The surface-limited degradation model predicts both the thickness and the in-plane shrinkage within 1.6% of the measured values, capturing lateral dissolution effects that existing one-dimensional formulations cannot represent. **Fig. 1F** shows dissolution experiments on 100-nm-thick Mg films in PBS. Patterns spelling "RICE," "UH," and the Rice University shield exhibit nonuniform dissolution profiles driven by local geometric variations, with narrower regions degrading faster than wider segments. The element-density simulations capture this behavior, reproducing the partial dissolution of the letters at 22.5 min, their complete disappearance at 27 min, and the anisotropic spatial diffusion evident in the university shield. **Supplementary Fig. 5** shows the density-based finite element mesh for the Rice University shield, highlighting the resolution and geometric fidelity. Additional dissolution experiments and simulations for 40-nm, 70-nm, and 100-nm-thick designs, shown in **Supplementary Figs. 6–8** and **Supplementary Movie 1**, demonstrate complete spatial degradation of the Mg films in PBS at room temperature over 25 minutes. The results reveal anisotropic spatial degradation driven by local curvature, feature width, and neighborhood connectivity, which together modulate in-plane diffusion paths and out-of-plane dissolution fronts. The density-field model, implemented with a 600 × 600 element mesh and a time step of $\Delta t = 0.005$ (**Supplementary Fig. 9**), accurately reproduces these anisotropic degradation patterns, including asymmetric edge retreat and accelerated dissolution in highly curved and narrowly connected regions.

Validation Against Theory and Analytical Scaling Laws

Prior work by Li et al. (2013) (28) established a reaction–diffusion framework for transient electronics that predicts the remaining mass of a dissolving material and the corresponding resistance per unit length of Mg conductors. The governing reactive-diffusion equation is

$$D\frac{\partial^2 w}{\partial y^2} - kw = \frac{\partial w}{\partial t} \tag{4}$$

Here, D and k denote the diffusion coefficient and reaction constant of the porous material–water system, and $w(y,t)$ is the local water concentration. A scaling analysis shows that the normalized concentration depends on three nondimensional groups: the normalized position $\frac{y}{h_0}$, the normalized time $\frac{Dt}{h_0^2}$, and reaction-diffusion ratio $\frac{kh_0^2}{D}$, such that

$$\frac{w}{w_0} = \widetilde{w}\left(\frac{y}{h_0}, \frac{Dt}{h_0^2}, \frac{kh_0^2}{D}\right) \tag{5}$$

A 3D finite element model evaluates the normalized weight loss and concentration fields within a Mg rectangular domain of 10 μm × 2.5 μm × 200 nm. The bottom face is prescribed a zero-concentration Dirichlet condition, allowing diffusion only through the remaining five surfaces of the prism. **Fig. 2A** shows that the bulk degradation model and the 3D diffusion simulation yield nearly identical normalized weight-loss kinetics, with deviations below 1%. Both models capture the rapid early-stage mass loss (~75% by normalized time t^*= 0.2), driven by high boundary concentration gradients, and the subsequent slowdown as these gradients decrease. The finite element results in **Fig. 2B** demonstrate this directly: concentration increases monotonically over time, but the kinetics slow as the internal diffusion gradients approach zero. The edge effects shown in **Fig. 2C** highlight the influence of 3D diffusion, which the bulk model reproduces accurately. As the nondimensional time increases from 0.1 to 1.0, the concentration field rises monotonically and progressively saturates the entire sample. **Supplementary Fig. 10** shows the sensitivity of the complete resorption time to $C_\perp$, $C_\parallel$, and the density-filter radius $R_{\min}$. Among these parameters, the out-of-plane degradation coefficient $C_\perp$exerts the strongest influence on dissolution behavior.

Validation against theoretical predictions highlights the differences of extending degradation analysis from 1D formulations to full 3D, system-level models. **Fig. 2D** illustrates two representative configurations for bioresorbable electronics: (i) a single porous Mg metal layer of thickness h_0, and (ii) a porous Mg metal layer encapsulated by MgO an additional material of total thickness $h_0 + h_{\text{encapsulation}}$ to prolong degradation. **Figs. 2E–F** show that the nondimensional concentration in the porous Mg layer increases monotonically as the normalized time rises from 0.05 to 2 (color gradient from black to blue). Incorporating an MgO layer slows degradation by reducing both the effective reaction rate and the diffusive accessibility of the Mg surface. In **Fig. 2F**, the analytical model predicts an asymptotic concentration plateau of ~ 0.1 at long times due to the imposed reaction–diffusion balance, whereas the bulk model continues to increase toward full saturation and ultimately complete dissolution. This divergence reflects the fundamental difference between a partially reactive, diffusion-limited interface and a fully resorbable system in which all solid material is eventually removed.

Transient Electrical Responses

Because bioresorbable electronics must maintain electrical functionality, such as stimulation or passive sensing, a critical quantity to predict is the time point at which circuit continuity is disrupted. **Fig. 3A** shows the normalized resistance $R(t)/R_0$ for five representative geometries: (i) a serpentine patch, (ii) a spiral, (iii) a serpentine interconnect (7), (iv) a square patch, and (v) a single rectangular strip. All exhibit the characteristic "J-shaped'' resistance evolution, computed from $R(t) = V/I(t)$, where V is the applied voltage and $I(t)$ is the dissolution-dependent current at the circuit terminals (see Methods for modeling details). Notably, the serpentine and square patches (green and orange curves), which incorporate hierarchical designs, exhibit a discrete jump in resistance. This jump corresponds to the dissolution of the first hierarchical layer, while the remaining layer preserves a continuous conductive path. This result highlights the importance of mapping dissolution pathways in bioresorbable electronics, as different regions fail at different times and govern the sequence of electrical disruption. **Fig. 3B** shows the normalized electric field (E-field) in three sequential states of each structure: initial, partially degraded, and fully disconnected. The spiral and serpentine geometries maintain a nearly uniform electric-field distribution throughout degradation, whereas the patch designs exhibit localized current pathways that reorganize after partial dissolution (normalized time > 0.3). This redistribution reflects the sequential degradation of hierarchical conductive networks while preserving circuit continuity. **Supplementary Movie 2** shows the simulated time-dependent degradation and corresponding electric-field evolution in all five structures. **Figs. 3C–E** show the evolution of the element-density field and the corresponding redistribution of the electric field in a 100 nm thick Mg biphasic neural probe immersed in PBS at room temperature. The design incorporates stretchable serpentine interconnects and eight square islands, analogous to previously reported rigid-island stretchable architectures (60). Experimental and simulation results in **Supplementary Fig. 11** show that the probe remains electrically connected for approximately 124 s despite progressive material loss. During this period, the resistance increases from ~140 Ω to ~900 Ω, corresponding to a >540% increase, while maintaining a continuous conductive pathway between the eight stimulation electrodes. Simulations reveal progressive localization of the electric field within the surviving serpentine interconnects as degradation reduces the effective conductive cross-sectional area. **Supplementary Movie 3** shows the complete dissolution process. Electrical failure occurs when dissolution removes the final conductive pathway, producing an abrupt transition "J-shape" to an open-circuit state.

Transient Electromagnetic and Radiofrequency Responses

Radiofrequency electronics provide an attractive platform for implantable systems because wireless readouts of resonant frequency and reflection coefficient (S_{11}) can serve as direct metrics of dissolution. A transient radiofrequency metamaterial resonator with dimensions 1.35 cm × 1.35 cm × 4 μm, as reported by Hwang et al. (2012) (53), is used to validate the model. **Fig. 3F** shows the mesh and evolution of the element-density field during dissolution of the resonator, revealing progressive thinning of the structure over time. Frequency-domain simulations in **Fig. 3G** capture the evolution of the radiofrequency response during degradation of the transient metamaterial resonator (E: Experiments, M: Model). At $t^* = 0$, the device exhibits a well-defined resonance near 1.8 GHz with a minimum S_{11} of approximately −6.5 dB. As degradation progresses, the resonance becomes progressively shallower, with the minimum S_{11} increasing to approximately −1.7 dB at $t^* = 1.0$, corresponding to a ~74% reduction in the reflection coefficient. The resonant frequency simultaneously decreases from ~1.80 GHz to ~1.65 GHz, an overall shift of approximately 8%. Experimental measurements from Hwang et al. (2012) (53) follow the same trends and show good agreement with the simulations throughout degradation. **Fig. 3H** summarizes the evolution of the minimum S_{11} and resonant frequency extracted from the spectra. The minimum S_{11} increases monotonically as degradation proceeds, indicating reduced coupling efficiency and increased resistive losses, whereas the resonant frequency exhibits a comparatively modest shift. Between $t^* = 1.0$ and $t^* = 1.8$, the resonant peak becomes indistinguishable from the background response as degradation eliminates the conductive pathways necessary to support resonance. The larger sensitivity of S_{11} reflects

the progressive reduction in effective conductivity and current-carrying cross-sectional area, while the resonant frequency remains governed primarily by the geometric inductance and capacitance of the resonator. Small discrepancies between model and experiment arise from nonuniform dissolution and local Mg thickness variations. Additional experimental uncertainty may result from impedance mismatch in the Tx–Rx system and small variations in relative coil positioning that were difficult to verify independently during degradation. These effects are expected to contribute primarily at late stages of resorption, when the quality factor decreases and the resonant response becomes increasingly sensitive to perturbations. Despite these uncertainties, the framework accurately reproduces the transient evolution of resonant frequency, reflection coefficient, and quality factor during degradation, demonstrating its utility for bioresorbable RF devices that operate through wireless coupling.

Transient Mechanical Responses (One Way Coupling)

Stretchable electronics for implantable applications commonly rely on serpentine interconnects to accommodate large deformations (**Fig. 4A**). These geometries reduce the overall system-level stiffness, enabling high stretchability when conforming to curved, dynamically moving biological surfaces, such as the epicardium, bladder, and gastrointestinal tract. Failure in stretchable interconnects is typically governed by excessive yield and eventual material fracture, but in bioresorbable systems, the dissolution of the traces introduces an additional, time-dependent failure pathway. Capturing the temporal evolution of circuit breakage, therefore, requires accounting for both mechanical strain and material degradation. We benchmark the model against commonly used hierarchical island–bridge architectures and outer serpentine–spiral circuits with lateral dimensions of 4.00 mm × 4.00 mm × 20 μm. **Fig. 4B** shows the resulting strain distribution under 20% axial stretch (ε_x), and a bending radius of $r = 3.75$ mm at key dissolution times. The maximum strain initiates at 1.5% in stretching and 0.7% in bending (for the deformed but degradation-free case) and increases steadily until $t^* = 0.30$, reaching 4.4% and 3.4%, respectively. **Fig. 4C** shows that this strain evolution results from the progressive reduction in stiffness of the constituent layers: as dissolution preferentially thins and softens the metal layer first, the local neutral axis shifts and load redistributes toward the remaining material, thereby increasing the strain in the remaining traces. Beyond $t^* = 0.30$, failure of these load-bearing pathways breaks the global load path, mechanically isolating the islands from the system. As a result, strain accumulation in the interconnects diminishes, reflecting a transition from a continuous, load-transmitting serpentine architecture to isolated islands whose deformation is governed primarily by the underlying substrate. **Fig. 4D** shows the force–displacement response of the stretchable circuit. In the degradation-free state, the network sustains forces up to 36 mN at a 2-mm displacement. As dissolution progresses, the effective stiffness of the serpentine interconnects decreases, reducing the load-carrying capacity to ~8 mN by $t^* = 0.30$, just prior to mechanical disconnection. Once the serpentine pathways are fully removed at $t^* = 0.35$, the structural topology collapses to isolated islands, and the force drops to ~6 mN, reflecting a system that no longer supports global deformation. Modeling of the effective axial and flexural stiffness (see Methods and **Supplementary Note 3**) reveals a strongly nonlinear decay with time. **Fig. 4E** shows that the axial stiffness decreases continuously toward zero as dissolution removes the load-bearing serpentine network, whereas the flexural stiffness asymptotically approaches ~0.25 kN·mm^2 due to the residual support provided by the underlying tissue. A sharp drop in both quantities occurs between $t^* = 0.30$ and $t^* = 0.35$, marking the point at which the interconnect topology collapses and the system transitions from a connected deformable network to mechanically isolated islands, consistent with the strain reduction observed in **Fig. 4C**.

The parametric design maps of a stretchable serpentine unit cell $l_{\text{unit}} = 4(l\sin\alpha + R\cos\alpha)$ in **Supplementary Fig. 12** reveal that, within the feasible design space excluding self-contact geometries, trace width is the primary determinant of functional lifetime, whereas larger radii and negative arc angles provide secondary increases in normalized disconnection time. Increasing w from 0.01 to 0.06 increases the normalized disconnection time from ~0.25–0.35 to ~0.75–0.90, corresponding to an approximate 2.5–

3-fold increase. Larger radii reduce curvature-driven localization of degradation, and negative arc angles increase the effective path length of the serpentine network. Together, these effects produce the longest normalized disconnection times for geometries satisfying $\alpha < -15°$, $w > 0.06$, $R > 0.07$, and $l > 0.10$. These results complement traditional stretchability-based optimization and provide a framework for engineering functional lifetime in bioresorbable stretchable electronics.

Transient Mechanical Responses (Two Way Coupling)

In highly deformable bioresorbable systems, such as those summarized in Table 1, mechanical loading can modify degradation kinetics through stress-assisted electrochemical processes, thereby coupling the mechanical response to material resorption. To capture this interaction, the framework is extended by allowing the degradation coefficients to vary with the local hydrostatic stress field (**Supplementary Fig. 13**), analogous to the stress-dependent modification of anodic current density reported in corrosion models (61, 62). The out-of-plane and in-plane degradation coefficients become

$$C_{\perp}^{*} = C_{\perp} \exp\left(\frac{\sigma_m V_m}{RT}\right) \tag{6}$$

$$C_{\parallel}^{*} = C_{\parallel} \exp\left(\frac{\sigma_m V_m}{RT}\right) \tag{7}$$

where σ_m is the hydrostatic stress, V_m is the molar volume, R is the universal gas constant, and T is the absolute temperature. Positive hydrostatic stress accelerates degradation by increasing the effective degradation coefficients, whereas regions subjected to lower stress evolve according to the baseline one-way formulation. This approach introduces simple mechanistic feedback between deformation and degradation without requiring additional empirical fitting parameters. **Supplementary Fig. 14** illustrates the influence of stress-assisted degradation on a representative serpentine interconnect subjected to uniaxial stretching. The hydrostatic stress field localizes near the outer surfaces of the serpentine arcs, producing spatially nonuniform amplification of the degradation coefficients through Eqs. (6–7). Consequently, degradation progresses preferentially in highly stressed regions, leading to asymmetric material loss compared with the one-way coupling formulation. The exponential stress dependence produces a monotonic increase in the effective degradation rate with applied strain, while recovering the one-way formulation in the undeformed state ($\sigma_m = 0$, $C_{\perp,\parallel}^{*} = C_{\perp,\parallel}$). The resulting density evolution exhibits progressively shorter functional lifetimes with increasing applied strain. Increasing the applied strain from 0% to 15% shifts the electrical disconnection point from $t^{*} \approx 0.48$ to $t^{*} \approx 0.18$, corresponding to an approximately 62% reduction in normalized functional lifetime. Intermediate strain levels of 5% and 10% produce disconnection at $t^{*} \approx 0.42$ and $t^{*} \approx 0.31$, respectively, demonstrating a systematic coupling between deformation and degradation. These results demonstrate that even moderate deformation within the elastic regime can alter degradation kinetics and functional lifetime, motivating the use of two-way coupling formulations for highly deformable bioresorbable electronic systems.

Transient Strain and Pressure Sensors

Strain and pressure sensors are central to bio-integrated systems because they transduce mechanical deformation into electrical signals that reflect tissue mechanics and correlate with physiological function. Here, we benchmark the system-level performance predicted by our model against the strain- and pressure-sensor geometries reported by Lu et al. (2012) (63). **Fig. 5A** shows an exploded view of the strain sensor, which incorporates two distinct serpentine patterns chosen to enable hierarchical degradation under separate longitudinal and transverse strain (20%). **Supplementary Movie 4** illustrates the time-dependent dissolution of the strain sensor. A voltage potential is applied across the sensor terminals to track the evolution of electrical resistance during degradation. **Fig. 5B** shows the strain

evolution in the deformed strain sensor. For the degradation-free layouts, the longitudinal case exhibits a nearly uniform strain field with a peak of ~3%, whereas the transverse case reaches a strain of ~5% at the straight segments due to the curvature-induced stress redistribution inherent to the layout orientation. As dissolution progresses to $t^* = 0.15$, stiffness loss in the serpentine traces increases the strain, reaching ~7% in the longitudinal orientation and ~12% in the transverse orientation. By $t^* = 0.35$, the central, thinner traces have fully degraded, removing key load-bearing paths and increasing strain localization exceeding 15% in both loading modes. **Fig. 5C-D** show the transient resistance change under longitudinal and transverse applied strains, respectively. Under longitudinal loading, the resistance change is negative and exhibits a nonlinear response determined by the sensor geometry. As dissolution progresses, the magnitude of the negative resistance change grows from 6.8% to 14.1% at 20% strain. Once the central serpentine traces disappear, the hierarchical layout produces a discrete jump to ~16% (red dashed curve), reflecting the loss of a parallel conductive path. Under transverse loading, the resistance change is positive, increasing from 17% to 39% at 20% strain. After the middle serpentines vanish, the resistance decreases slightly to ~36% because the structural loss reduces overall conductivity, even though transverse loading would otherwise favor a positive gauge response (i.e., electric-field and strain directions remain orthogonal). The insets in **Fig. 5C-D** show the corresponding finite element strain fields after the central serpentine has dissolved. The sensitivity is captured using the gauge factor (GF) as:

$$GF = \frac{\Delta R}{R\varepsilon_{app}} \tag{8}$$

Where ΔR is the resistance change, R is the original resistance, and ε_{app} is the applied strain. **Fig. 5E** shows the temporal evolution of GF as the sensors dissolve. The transverse GF is positive and increases from 0.8 to 1.8, whereas the longitudinal GF is negative and decreases from –0.4 to –0.8. Once the central serpentine fully degrades, the GF drops in both loading modes due to the loss of the dominant conductive path. This behavior is particularly relevant for implantable systems, where in vivo characterization is difficult or, in some cases, inaccessible. Discrete changes in GF caused by hierarchical dissolution provide a clear electrical signature of partial subsystem failure within the larger bioelectronic platform, offering a practical indicator of remaining lifetime and functional integrity.

Figures 5F–G demonstrate the application of the framework to a bioresorbable Mg pressure sensor integrated onto a biomimetic bladder (see Methods and **Supplementary Fig. 15** for microfabrication details). The sensor consists of a serpentine Mg conductor designed to accommodate large deformations while maintaining electrical continuity during inflation from 1 mL to 2 mL (**Supplementary Fig. 16**). Internal bladder pressure generates mechanical strain in the serpentine trace, resulting in a measurable increase in electrical resistance. As degradation progresses, material loss reduces the effective conductive cross-sectional area, causing the electromechanical response to become increasingly sensitive to pressure. The pressure–resistance transitions from linear to non-linear over the investigated pressure range (0–20 kPa) and exhibits a pronounced increase in sensitivity with degradation time. The sensitivity increases from approximately 0.20 % kPa^{-1} in the undegraded state to ~0.35 % kPa^{-1} after 2 min, ~0.50 % kPa^{-1} after 3 min, ~0.65 % kPa^{-1} after 5 min, and ~0.90 % kPa^{-1} after 8 min of dissolution, corresponding to an overall increase of more than fourfold. At a pressure of 20 kPa, the resistance change increases from approximately 4% in the pristine device to approximately 18% after 8 min of degradation. These results demonstrate that degradation not only reduces the remaining functional lifetime of the device but also continuously modifies its sensing characteristics. The simulations accurately reproduce both the magnitude and temporal evolution of the electromechanical response. Agreement is strongest during the early stages of degradation (0–3 min), where the predicted pressure sensitivities closely match experimental measurements and the degradation remains spatially uniform. At later stages (5–8 min), the model slightly underestimates the resistance change observed experimentally. For example, at 20 kPa and 8 min, the simulations predict a resistance increase of approximately 15%, compared with ~18% measured

experimentally. This discrepancy likely arises from localized dissolution, edge roughening, stochastic material loss, and geometric imperfections that are not fully captured by the homogenized density-field representation.

Further modeling demonstrations of pressure sensors, in **Fig. 6A**, show the utility of transient mechanical responses to track physiological signals. For a serpentine-based pressure sensor embedded in soft tissue, inspired by designs reported by Lu et al. (2012) (63), we apply pressures from 0–20 kPa. In the undegraded state, the resistance change reaches approximately 22% at 20 kPa. After 8 min of dissolution, the resistance change increases to approximately 58%, corresponding to a ~2.6-fold amplification of the sensing response. The pressure sensitivity in therefore increases from ~1.1% kPa^{-1} to ~2.9% kPa^{-1} over the degradation period. The simulations in **Fig. 6B** accurately reproduce both the magnitude and non-linearity of the experimental response across the entire pressure range. At intermediate pressures (10–15 kPa), the predicted resistance changes differ from experimental measurements by only a few percentage points, while the overall trends remain consistent throughout degradation. The model overpredicts (absolute difference of ~10 percentage points, or a relative overprediction of ~50%) the resistance changes at intermediate pressures (6–15 kPa), while maintaining good agreement at both low and high pressures. This discrepancy likely arises from simplifications in the mechanical representation of the bladder–sensor interface. The simulations assume ideal adhesion and uniform strain transfer between the expanding elastomer and the Mg sensor, whereas experimental measurements may exhibit localized strain relaxation, interfacial compliance, and small variations in bonding that reduce the effective strain transmitted to the conductive trace. The optical image in **Fig. 6C** and finite element simulations in **Fig. 6D** show that degradation increases the out-of-plane compliance of the serpentine structure over 4 min of dissolution producing local strain concentrations exceeding 10%, leading to larger resistance changes and enhanced pressure sensitivity.

Figures 6E–G illustrate the experimental characterization platform. A bioresorbable Mg pressure sensor was integrated onto a biomimetic bladder and immersed in PBS to induce hydrolytic degradation. The resulting Mg dissolution is spatially heterogeneous, with localized thinning and material loss evident after 15 min, providing a simplified representative experimental system for validating the predicted evolution of sensor functionality during bioresorption. **Supplementary Fig. 17** shows time-dependent simulations of the strain and pressure sensors, capturing the characteristic "J-shaped" resistance response and the discrete resistance jumps in the strain sensor. Together, these results highlight the strong predictive capability of the model across distinct sensing modalities. As a practical *in-silico* demonstration, we model the response of a transient pressure sensor subjected to a 10-s ECG waveform (see **Supplementary Note 4** for the waveform definition). **Fig. 6H** shows that the resistance change reproduces the pressure pattern, with distinct peaks corresponding to the ECG cycle. As the sensor degrades, the response is amplified, with peak resistance changes increasing by ~30% at $t = 2$ min and ~50% at $t = 6$ min, reflecting the amplified mechanical compliance and strain sensitivity changes by dissolution. **Supplementary Movie 4** shows the predicted degradation of system-level circuit architectures for stretchable electronics. These predictions highlight a distinct utility of transient sensors: their functional response is intrinsically linked to their degradation timescale, enabling devices that do not simply persist until resorption but remain operational, and in some cases increasingly responsive/sensitive, throughout their dissolution period.

System-Level Transient Modeling

To demonstrate the utility of the framework in a clinically relevant setting, we adopt the architecture of a previously reported bioresorbable cardiac pacing system (6), consisting of wireless power harvesting coils, stretchable interconnects, and stimulation electrodes. Longitudinal CT imaging of implanted devices in rats reveals progressive resorption of the metallic components over a period of approximately 9 weeks, culminating in complete disappearance of the electrode structures by day 62 (**Fig. 7A**). This

system provides a representative example for evaluating how spatially heterogeneous degradation influences electromagnetic, electrical, and mechanical functionality in bioresorbable implantable electronics. **Figures 7B**(i–iv) illustrate the application of the framework to a bioresorbable cardiac pacing system composed of metallic conductors and polymer encapsulation layers that degrade on distinct timescales. Accelerated in vitro dissolution studies show substantial loss of the metallic components by day 20 and complete disappearance of the d-CDPU encapsulation by day 40. The density-field simulations reproduce the progressive spatial evolution of both material systems and model the corresponding mechanical response throughout degradation. At day 0, the applied strain ($\varepsilon_{\mathrm{app}} = 15\%$) is distributed between the Mo conductors and the surrounding d-CDPU substrate. The highest strains are within the serpentine interconnect region, where the geometry accommodates the imposed deformation. The maximum strain in the Mo remains below approximately 0.5%, while the d-CDPU experiences localized strains approaching 30%, consistent with the intended strain-isolation strategy of stretchable electronics. As degradation progresses, the load-bearing architecture evolves substantially. By day 20, degradation of the metallic network reduces the effective stiffness of the interconnects and alters the distribution of strain throughout the device. The simulations show a progressive transfer of deformation from the metallic components to the polymeric substrate as conductive pathways disappear. By day 40, the metallic traces have completely resorbed, and the remaining deformation is carried exclusively by the d-CDPU structure.

Importantly, the framework captures not only the spatial progression of material loss but also the resulting redistribution of mechanical fields throughout degradation. Such functional information is difficult to obtain experimentally because strains within encapsulated or partially resorbed conductors cannot be measured directly during the degradation process, particularly in implantable systems. The simulations reveal how degradation progressively alters structural compliance, load transfer, and strain localization as different material constituents disappear at different rates. The framework is further applied to a frequency-selective wireless heating resonator proposed by Rüegg et al. (43), consisting of a circular resonator integrated with a localized meandered microheater. The geometry intentionally concentrates induced currents within the microheater region, producing localized electromagnetic fields that enable wireless heating. The simulations predict progressive degradation of the meandered conductor, beginning at regions of high current density and evolving toward complete electrical disconnection at $t^* = 0.28$. As material resorption proceeds, the electromagnetic field distribution becomes increasingly localized within the remaining conductive pathways before the resonant current path is interrupted entirely (**Supplementary Fig. 18**). These results demonstrate the ability of the framework to resolve how spatially heterogeneous degradation modifies both device architecture and electromagnetic functionality in transient therapeutic systems.

Discussion

Bioresorbable electronics challenge conventional device design, which typically optimizes performance at the intact or initial state, because operation in physiological or other chemical environments induces continuous material resorption that alters structural and electrical behavior over time. Unlike permanent systems, transient devices function under evolving boundary conditions in which geometry, material properties, and connectivity change concurrently with performance. Predicting operational lifetime therefore requires resolving how degradation interacts with geometry, topology, and multiphysics at the system level. One-dimensional reactive–diffusion models estimate dissolution time from thickness loss but do not capture three-dimensional current pathways, load redistribution, or failure localization in functional and deformable circuits. In practical systems, operation ceases when a critical conductive or load-bearing pathway is disrupted, not just when material volume vanishes. A functional lifetime defined solely by complete dissolution, therefore, overestimates usable performance. By embedding degradation within a spatially resolved electromechanical framework, the present model links dissolution kinetics directly to evolving functional metrics and defines lifetime in terms of performance thresholds.

A central finding is the existence of a pre-failure regime in which performance evolves prior to disconnection. Early and intermediate degradation produces localized thinning that modifies stiffness, resistance, and strain distribution without structural separation. These changes alter calibration, sensitivity, and impedance matching before terminal device failure. Because stress and current density concentrate near partially degraded regions (**Figure 3**), the response may be nonmonotonic. Devices can remain electrically continuous yet functionally unstable. For physiological sensing, electrotherapy, or wireless communication, such drift may limit accuracy even when structural elements remain functional. Circuit topology governs the onset and abruptness of functional failure. Hierarchical and serpentine interconnects tolerate uniform thinning but exhibit rapid transitions when specific pathways degrade. Parametric studies of stretchable serpentines (**Supplementary Fig. 12**) demonstrate that geometry controls both mechanical performance and degradation failure. Serpentine geometries that distribute strain over longer conductive pathways delay electrical disconnection and extend functional lifetime, highlighting opportunities to co-design stretchability and bioresorption behavior.

Failure, therefore, depends on network connectivity rather than the remaining material fraction. This behavior enables two design strategies: increasing electrical connectivity to extend functional lifetime or intentionally programming weakest-path disruption to achieve staged dissolution or time-sequenced functionality. Degradation thus becomes a critical design variable that was previously unaccounted for. Distinct physical regions reach failure thresholds at different times. Electrical resistance and mechanical stiffness respond to early-stage material loss, whereas wireless performance persists longer because resonance depends primarily on geometric configuration and inductive–capacitive coupling. A single bioresorbable system can therefore exhibit domain-specific functional lifetimes. Future classification of bioresorbable device must reflect this separation from its constitutive materials, with independent performance criteria for mechanical integrity, electrical conduction, and electromagnetic response. Multiphysics analysis is necessary for integrated deformable platforms that combine sensing, actuation, and communication. Mechanics additionally provides a first-order criterion to determine whether deformation alters electrochemical response and resorption timescales. Two-way coupling reveals that an applied axial strain of 15% reduces the normalized functional lifetime of serpentine interconnects by approximately 62%, highlighting the influence of mechanical deformation on degradation kinetics.

Several limitations define the current scope. The present formulation assumes one-way coupling and a simplified two-way coupling between degradation and mechanical fields. *In vivo* conditions may additionally introduce stress-assisted corrosion, temperature-dependent kinetics, fluid transport, pH

variations, ionic composition, and biofouling, each of which can modify reaction rates by several orders of magnitude. Because the proposed framework is material agnostic, effective diffusion and reaction coefficients for organic and inorganic constituents can, in principle, be calibrated using Arrhenius-type relations for chemical kinetics (3, 46), while mechanics damage formulations can be incorporated to capture progressive material failure. The predictive accuracy of these extensions, however, depends strongly on the availability and quality of experimental characterization data.

The model implementation emphasizes two-dimensional representations for computational efficiency and does not fully capture out-of-plane fracture or three-dimensional current flow relevant to thicker or multilayer devices. Constitutive properties of partially degraded regions are introduced through parameterization. Systematic and reproducible experimental characterization of evolving conductivity and elastic modulus in magnesium, molybdenum, zinc, tungsten, and related materials will improve quantitative predictive accuracy, particularly in regimes governed by two-way coupling. These constraints define the regime in which the modeling framework provides reliable design guidance.

Translation to clinical systems requires system-level validation under coupled mechanical, chemical, and physiological loading conditions. Existing studies demonstrate that *in vivo* degradation rates can differ substantially from *in vitro* measurements, often by factors of two to six depending on the material system and implantation environment. Such localization and variability further motivate predictive frameworks capable of linking evolving material architectures to device functionality. Future developments that incorporate three-dimensional geometries, triggered degradation strategies, encapsulation layers, and physiologically calibrated degradation kinetics will enable increasingly realistic predictions of system-level performance.

By resolving how spatially heterogeneous material evolution reshapes electromechanical and electromagnetic responses in real time, the framework establishes a foundation to evaluate functionality in bioresorbable electronics. First, it captures spatial degradation pathways, including both thickness reduction and lateral geometric evolution, across a broad range of flexible and stretchable electronic architectures. Second, it quantifies the corresponding evolution of mechanical fields, including stress, strain, and displacement, together with electrical fields, including voltage and current density, throughout the degradation process. Device lifetime becomes a controllable design parameter defined by performance thresholds rather than material disappearance alone. This capability is central to future transient implants and time-limited therapeutic systems in which predictable functional evolution, not merely eventual resorption, determines clinical value.

Methods

Microfabrication of the Experimental Mg patterns

A series of patterned structures—including the words "RICE" and "UH", the Rice University shield, a 3 x 3 electromyography (EMG) sensor array and biphasic strip stretchable electronics with serpentine interconnects were designed in AutoCAD 2024 and fabricated using a standard lift-off process. Fused silica wafers (500 μm thick, double-side polished) were spin-coated with a 9 μm layer of positive-tone photoresist (AZ12XT) using a Brewer Cee 200X spin coater. Photolithography was performed using a mask aligner (ABM Mask Aligner) with 365 nm ultraviolet exposure for 13.3 s, corresponding to an energy dose of 120 mJ cm^{-2}. After exposure, the samples were baked at 90 °C for 1 min in a vacuum oven and developed in AZ 300 MIF for 2 min at room temperature. Magnesium films with thicknesses of 40 nm, 70 nm, and 100 nm were deposited by magnetron sputtering (AJA ATC-2200). Lift-off was performed by immersing the samples in acetone, followed by ultrasonication in a water bath for 5 min at room temperature, which removed residual photoresist and defined the final pattern geometries. Film thickness and uniformity were quantified using a stylus profilometer (Dektak XT). The patterned samples were immersed in phosphate-buffered saline without calcium or magnesium (Dulbecco formulation, DPBS, CellPro Premium Labware) and incubated at 37 °C on a temperature-controlled hotplate (Guardian 5000, OHAUS Co). Optical images were acquired at 2-s intervals using a digital camera (Canon EOS90D DSLR) to track the temporal evolution of Mg degradation. For electrical characterization, a separate 100-nm-thick Mg sample containing the biphasic strip with serpentine interconnects was immersed in phosphate-buffered saline at room temperature. Electrical resistance between adjacent electrodes was measured at 1-min intervals. Open-circuit behavior occurred after approximately 3 min, consistent with the degradation trends reported in this study. **Supplementary Fig. 19** summarizes the complete set of patterned geometries explored in this work.

Microfabrication of the Experimental Stretchable Sensor

Bioresorbable magnesium (Mg) sensors were fabricated using photolithography, magnetron sputtering, and transfer-printing. A sacrificial layer of poly(methyl methacrylate) (PMMA) was first spin-coated onto a fused silica wafer, followed by a 5 μm thick polyimide (PI) layer. Photolithography defined the sensor geometries using a 9 μm thick positive-tone photoresist (AZ12XT) patterned with a maskless aligner (MLA150, Heidelberg Instruments). Magnesium was deposited by magnetron sputtering (AJA ATC-2200), and lift-off in acetone yielded the final Mg patterns. A top PI encapsulation layer was then applied, followed by deposition of a 60 nm silicon dioxide (SiO_2) layer by electron beam evaporation to enable covalent bonding during transfer printing. Separately, an Ecoflex elastomer substrate (Ecoflex 00-20 FAST, Smooth-On) was prepared on a PMMA-coated silicon wafer. Both the Ecoflex substrate and the SiO_2-coated Mg devices were treated with ultraviolet-ozone radiation for 5 min and immediately laminated together. Thermal treatment at 70 °C for 10 min promoted siloxane bond formation across the interface. The assembly was subsequently immersed in acetone at 80 °C to dissolve the PMMA sacrificial layer, enabling transfer of the encapsulated Mg devices onto the Ecoflex substrate. Reactive ion etching (RIE180, Oxford Instruments) with sulfur hexafluoride (SF_6) and oxygen (O_2) removed the exposed PI regions, using the Mg layer as a hard mask. The resulting structures consisted of flexible and stretchable Mg sensors embedded within thin PI/Ecoflex support layers.

Experimental Characterization of Transient Pressure Sensor

A biomimetic elastomeric bladder was fabricated by molding Ecoflex into a spherical geometry with a diameter of 10 mm and an initial volume of approximately 0.6 mL. The bioresorbable Mg sensors were laminated onto the outer surface of the bladder using uncured Ecoflex as an adhesive layer and allowed to cure at room temperature. The bladder was connected to a syringe pump (NE-1000, New Era Pump Systems) for controlled fluid infusion and to a pressure acquisition system (PowerLab, ADInstruments) for simultaneous measurement of internal pressure. Inflation experiments were performed by increasing the fluid volume in increments of 0.2 mL at a constant flow rate of 0.2 mL min^{-1}. The initial volume was

1 mL for strip-type sensors and 4 mL for strain-gauge sensors. Electrical resistance and internal pressure were recorded at each volume increment to establish the electromechanical response of the devices. To evaluate transient performance during degradation, the integrated Mg sensor–bladder assemblies were immersed in phosphate-buffered saline (PBS) for prescribed durations of 1 and 2 min. Following each immersion interval, the inflation protocol was repeated and the resistance–pressure response was measured. These experiments quantified the evolution of sensor performance as a function of hydrolytic degradation time.

FEM – degradation model

An in-house explicit time-integration code for system-level degradation was implemented in MATLAB. The formulation employed a density-based finite element approach, in which each element was assigned a normalized material density $\rho_e \in [0,1]$ to represent the evolving material state. Numerical stability constrains the allowable time step in the explicit degradation formulation. Large time increments introduce numerical instability in the bulk-degradation regime (Supplementary Fig. 3). To ensure stable temporal integration, the time step satisfies a criterion consistent with the Courant–Friedrichs–Lewy (CFL) condition

$$\Delta t < \frac{1}{2D\left(\frac{1}{\Delta x^2} + \frac{1}{\Delta y^2}\right)} \tag{9}$$

where Δx and Δy denote the minimum element dimension and D is the diffusion coefficient. For structured meshes, this reduces to $\Delta t = \mathcal{O}(h^2/D)$, where h is the characteristic element size. Convergence is established by progressively reducing Δt until additional refinement produces negligible changes in the density evolution, electrical response, and failure metrics. To maintain physical consistency during degradation, the formulation additionally enforces a non-negativity constraint on the density field through the explicit update.

$$\rho_{e,i+1} = \max\left(\rho_{e,i} - \left.\frac{d\rho_e}{dt}\right|_i \Delta t, 0\right) \tag{10}$$

which prevents nonphysical negative densities during temporal integration.

The complete formulation, numerical workflow, and algorithmic implementation are provided in **Supplementary Note 1** and **Supplementary Fig. S1.** Mesh discretization details are shown in **Supplementary Fig. S5.** Convergence studies with respect to element size and time-step resolution were performed to ensure numerical accuracy and stability, with results summarized in **Supplementary Fig. S9.** The coupled degradation–mechanical–electrical problem was implemented using a one-way coupling strategy: degradation evolved independently of mechanical deformation and electrical loading, while the evolving material density informed the subsequent mechanical and electrical analyses. All geometric parameters used in this study are summarized in **Supplementary Fig. S19**, and all degradation-related material and kinetic parameters are listed in **Supplementary Table 2**. A simple extension of the framework to account for two-way coupling is presented in **Supplementary Fig. 13**, where stress-assisted degradation in the elastic regime is incorporated through the local hydrostatic pressure field, which modifies the coefficient $C_\perp$ and $C_\parallel$ in Eq. (3).

FEM – mechanics model

Mechanical models of system-level electronic circuits were performed using a commercial finite element package (ABAQUS 2023). An in-house Python scripting workflow was developed to generate degraded circuit geometries by directly updating element-wise material properties based on the evolving density field from the degradation model. Four-node reduced-integration shell elements (S4R) were used to model

both the Mg metal circuits and the thin elastomeric substrate. The surrounding biological tissue was modeled using eight-node three-dimensional solid elements with a hybrid formulation (C3D8RH) to accommodate near-incompressibility. Mesh refinement studies were conducted to ensure numerical accuracy, yielding ~1,000,000 elements per electronic circuit simulation. Identical mesh discretizations were used for the mechanical, electrical, and degradation analyses to maintain consistency and nodal connectivity across coupled simulations. NLGEOM is enabled to account for geometrical nonlinearities under large deformation. The magnesium traces were modeled as linear elastic material with an elastic modulus $E_{\mathrm{Mg}} = 42$ GPa and Poisson's ratio $v_{\mathrm{Mg}} = 0.34$. Both the substrate and tissue layers were modeled using a Mooney–Rivlin hyperelastic constitutive model with parameters $C_{10} = 0.060$ MPa, $C_{01} = 0.015$ MPa, and $D = 0.4625$ MPa^{-1}. For the devices shown in **Figs. 4**, the substrate thickness was 20 μm, the magnesium layer thickness was 500 nm, and the tissue thickness was 0.04 mm; the tissue layer was included only in bending simulations. For the devices shown in **Figs. 5-6**, the substrate thickness was 20 μm, the magnesium thickness was 1 μm, and the tissue thickness was 5 mm. Following mechanical deformation, the nodal coordinates and strain tensors for each element were exported to MATLAB for subsequent electrical simulations. The deformed thickness of each element was computed as

$$t_e^{def} = t_e\left[1 - \frac{v}{1-v}\left(\varepsilon_{xx} + \varepsilon_{yy}\right)\right] \tag{11}$$

where the relation follows from a plane-stress assumption for a thin film undergoing in-plane strains ε_{xx} and ε_{yy} and t_e is the undeformed element thickness.

FEM – electrical resistance model

At each time step of the transient degradation simulation, an electrical current analysis was performed to evaluate the instantaneous circuit resistance. To enable efficient coupling with the degradation framework, an in-house finite element solver was implemented in MATLAB to solve the quasi-static current-conduction problem. The electrical domain was discretized using bilinear four-node quadrilateral elements (Q4) in an isoparametric formulation with full Gauss integration. Dirichlet voltage boundary conditions of 1 V and 0 V were prescribed at the circuit terminals. The total current was computed by integrating the normal current flux over the electrode boundaries, and the circuit resistance was obtained from the applied voltage and resulting current. Model accuracy was verified by benchmarking against simulations performed using a commercial multiphysics finite element package (COMSOL). For the thin electronic films, the electrical formulation accounted for three coupled effects: conductivity reduction due to material degradation, in-plane strain-induced changes in electrical response, and out-of-plane thickness evolution computed from the plane-stress relation in Eq. (11). These contributions were updated consistently at each time step to capture the coupled Multiphysics response of the degradable circuit.

FEM – electromagnetic antenna modeling

Electromagnetic simulations of the bioresorbable radiofrequency (RF) metamaterial antennas were performed using a commercial finite-element solver (ANSYS HFSS). The simulations resolved the time-dependent evolution of the resonant frequency, unloaded quality factor (Q), and reflection coefficient (S_{11}) during degradation. The antenna geometry followed a previously reported bioresorbable design (Hwang et al., 2012) and consisted of a copper transmitting (Tx) coil with an outer diameter of approximately 20 mm and a magnesium receiving (Rx) metamaterial antenna with dimensions of 1.35 cm × 1.35 cm × 4 μm. The separation between the Tx and Rx coils was fixed at 0.8 mm. Excitation was applied via a lumped port at the Rx antenna feed location. Perfect electric conductor (PEC) boundaries were assigned to the metallic traces, and additional PEC segments were introduced within the inner loops of the RF metamaterial antenna to enforce a well-defined current path and ensure stable port excitation. Open-region radiation conditions were imposed using a spherical radiation boundary with a radius of 1,000 mm, sufficiently large to minimize boundary reflections and approximate free-space propagation. An auto-adaptive tetrahedral mesh was used for all simulations, with local mesh refinement concentrated

near the metallic traces and regions of high field gradients. Mesh convergence was automatically verified in HFSS using energy residual criteria. Frequency-domain simulations were conducted over 1 GHz to 3 GHz to capture the antenna's resonant behavior and impedance response. Outputs from the degradation simulations were incorporated into the electromagnetic model by updating the effective electrical conductivity of the magnesium traces based on the evolving element-density field, while the antenna geometry and excitation conditions remained fixed. The reflection coefficient S_{11} was obtained directly from the lumped-port solution. The resonant frequency f_0 was identified from the minimum of the S_{11} spectrum, and the unloaded quality factor was computed using the −3 dB bandwidth definition $Q = \frac{f_0}{f_1 - f_2}$, where f_2 and f_1 are the upper and lower 3dB frequencies. Magnesium traces were modeled with relative permittivity $\varepsilon_{\mathrm{Mg}} = 1$ and a degradation-dependent electrical conductivity with an initial value of $\sigma_{\mathrm{Mg}} = 2.25 \times 10^7\ \mathrm{S\,m^{-1}}$. Copper traces in the transmitting coil were assigned $\varepsilon_{\mathrm{Cu}} = 1$ and $\sigma_{\mathrm{Cu}} = 5.8 \times 10^7\ \mathrm{S\,m^{-1}}$.

Data Availability: All study data are included in the article and/or SI Appendix.

Acknowledgments
Raudel Avila gratefully acknowledges support from the ASME Applied Mechanics Division Haythornthwaite Research Initiation Grant. R.A. acknowledged support from the Rice Office of Research & the Rice Brain Institute DPRIT Seed Grant Program. Z.L. acknowledges the support from the National Institute of Biomedical Imaging and Bioengineering of the National Institutes of Health under Award Number R21EB037317. This work made use of facilities and/or instrumentation supported by the Shared Equipment Authority at Rice University.

Author contributions:

Conceptualization: PL, RA
Methodology: PL, AG, ZL, RA
Investigation: PL, AG, ZL, RA
Visualization: PL, RA
Supervision: ZL, RA
Writing—original draft: PL, AG, ZL, RA
Writing—review & editing: RA

Competing interests: The authors declare no competing financial or non-financial interests.

References

1. P. Liu, C. Lee, N. Carusetta, R. Avila, Transient Mechanics: A Perspective on Bioresorbable Electronics. *J. Appl. Mech.* **92**, 051007 (2025).

2. Y. Zhang, *et al.*, Advances in Bioresorbable Materials and Electronics. *Chem. Rev.* **123**, 11722–11773 (2023).

3. S.-W. Hwang, *et al.*, 25th Anniversary Article: Materials for High-Performance Biodegradable Semiconductor Devices. *Adv. Mater.* **26**, 1992–2000 (2014).

4. G.-J. Ko, *et al.*, Materials and Designs for Extremely Efficient Encapsulation of Soft, Biodegradable Electronics. *Adv. Funct. Mater.* **34**, 2403427 (2024).

5. Y. S. Choi, *et al.*, Fully implantable and bioresorbable cardiac pacemakers without leads or batteries. *Nat. Biotechnol.* **39**, 1228–1238 (2021).

6. Y. S. Choi, *et al.*, A transient, closed-loop network of wireless, body-integrated devices for autonomous electrotherapy. *Science* **376**, 1006–1012 (2022).

7. H. Ryu, *et al.*, Materials and Design Approaches for a Fully Bioresorbable, Electrically Conductive and Mechanically Compliant Cardiac Patch Technology. *Adv. Sci.* **10**, 2303429 (2023).

8. J. H. Lim, *et al.*, Synthesis of shape-programmable elastomer for a bioresorbable, wireless nerve stimulator. *Biosens. Bioelectron.* **254**, 116222 (2024).

9. G. Lee, *et al.*, A bioresorbable peripheral nerve stimulator for electronic pain block. *Sci. Adv.* **8**, eabp9169 (2022).

10. Y. S. Choi, *et al.*, Stretchable, dynamic covalent polymers for soft, long-lived bioresorbable electronic stimulators designed to facilitate neuromuscular regeneration. *Nat. Commun.* **11**, 5990 (2020).

11. D.-M. Lee, *et al.*, An on-demand bioresorbable neurostimulator. *Nat. Commun.* **14**, 7315 (2023).

12. J. T. Reeder, *et al.*, Soft, bioresorbable coolers for reversible conduction block of peripheral nerves. *Science* **377**, 109–115 (2022).

13. J.-Y. Bae, *et al.*, A biodegradable and self-deployable electronic tent electrode for brain cortex interfacing. *Nat. Electron.* **7**, 815–828 (2024).

14. J. Koo, *et al.*, Wirelessly controlled, bioresorbable drug delivery device with active valves that exploit electrochemically triggered crevice corrosion. *Sci. Adv.* **6**, eabb1093 (2020).

15. Y. Huang, *et al.*, Implantable Electronic Medicine Enabled by Bioresorbable Microneedles for Wireless Electrotherapy and Drug Delivery. *Nano Lett.* **22**, 5944–5953 (2022).

16. R. Kaveti, *et al.*, Soft, Long-Lived, Bioresorbable Electronic Surgical Mesh with Wireless Pressure Monitor and On-Demand Drug Delivery. *Adv. Mater.* **36**, 2307391 (2024).

17. J. Lee, *et al.*, Flexible, sticky, and biodegradable wireless device for drug delivery to brain tumors. *Nat. Commun.* **10**, 5205 (2019).

18. Y. Zhang, *et al.*, Self-powered, light-controlled, bioresorbable platforms for programmed drug delivery. *Proc. Natl. Acad. Sci.* **120**, e2217734120 (2023).

19. C. H. Lee, *et al.*, Biological lipid membranes for on-demand, wireless drug delivery from thin, bioresorbable electronic implants. *NPG Asia Mater.* **7**, e227–e227 (2015).

20. Y. Zhang, *et al.*, Millimetre-scale bioresorbable optoelectronic systems for electrotherapy. *Nature* **640**, 77–86 (2025).

21. H. Ouyang, *et al.*, A Bioresorbable Dynamic Pressure Sensor for Cardiovascular Postoperative Care. *Adv. Mater.* **33**, 2102302 (2021).

22. A. Palmroth, *et al.*, Materials and Orthopedic Applications for Bioresorbable Inductively Coupled Resonance Sensors. *ACS Appl. Mater. Interfaces* **12**, 31148–31161 (2020).

23. J. Shin, *et al.*, Bioresorbable pressure sensors protected with thermally grown silicon dioxide for the monitoring of chronic diseases and healing processes. *Nat. Biomed. Eng.* **3**, 37–46 (2019).

24. Z. Li, C. Li, Y. Deng, Bioresorbable Pressure Sensor and Its Applications in Abnormal Respiratory Event Identification. *ACS Appl. Electron. Mater.* **5**, 1761–1769 (2023).

25. C. M. Boutry, *et al.*, A stretchable and biodegradable strain and pressure sensor for orthopaedic application. *Nat. Electron.* **1**, 314–321 (2018).

26. J. Liu, *et al.*, Bioresorbable shape-adaptive structures for ultrasonic monitoring of deep-tissue homeostasis. *Science* **383**, 1096–1103 (2024).

27. S. Li, *et al.*, Bioresorbable, wireless, passive sensors for continuous pH measurements and early detection of gastric leakage. *Sci. Adv.* **10**, eadj0268 (2024).

28. R. Li, *et al.*, An Analytical Model of Reactive Diffusion for Transient Electronics. *Adv. Funct. Mater.* **23**, 3106–3114 (2013).

29. R. Jamshidi, S. Çinar, Y. Chen, N. Hashemi, R. Montazami, Transient bioelectronics: Electronic properties of silver microparticle-based circuits on polymeric substrates subjected to mechanical load. *J. Polym. Sci. Part B Polym. Phys.* **53**, 1603–1610 (2015).

30. S. Çınar, R. Jamshidi, Y. Chen, N. Hashemi, R. Montazami, Study of mechanics of physically transient electronics: A step toward controlled transiency. *J. Polym. Sci. Part B Polym. Phys.* **54**, 517–524 (2016).

31. H. Cheng, V. Vepachedu, Recent development of transient electronics. *Theor. Appl. Mech. Lett.* **6**, 21–31 (2016).

32. M. Liu, *et al.*, The external stress-assisted corrosion behavior of Mg alloys for biomedical applications. *Corros. Sci.* **249**, 112856 (2025).

33. Y. Koo, Y. Jang, Y. Yun, A study of long-term static load on degradation and mechanical integrity of Mg alloys-based biodegradable metals. *Mater. Sci. Eng. B* **219**, 45–54 (2017).

34. X.-N. Gu, *et al.*, The effect of tensile and fluid shear stress on the in vitro degradation of magnesium alloy for stent applications. *Bioact. Mater.* **3**, 448–454 (2018).

35. Q. Yang, *et al.*, Ecoresorbable and bioresorbable microelectromechanical systems. *Nat. Electron.* **5**, 526–538 (2022).

36. K. J. Yu, *et al.*, Bioresorbable silicon electronics for transient spatiotemporal mapping of electrical activity from the cerebral cortex. *Nat. Mater.* **15**, 782–791 (2016).

37. M. Hjort, *et al.*, In situ assembly of bioresorbable organic bioelectronics in the brain. *Nat. Commun.* **14**, 4453 (2023).

38. J.-H. Lee, *et al.*, A Fully Biodegradable and Ultra-Sensitive Crack-Based Strain Sensor for Biomechanical Signal Monitoring. *Adv. Funct. Mater.* **34**, 2406035 (2024).

39. J. Park, *et al.*, A Bioresorbable Neural Interface for On-Demand Thermal Pain Block. *Adv. Funct. Mater.* **36**, e30035 (2026).

40. H.-Y. Ahn, *et al.*, Bioresorbable, wireless dual stimulator for peripheral nerve regeneration. *Nat. Commun.* **16**, 4752 (2025).

41. J. W. Song, *et al.*, Bioresorbable, wireless, and battery-free system for electrotherapy and impedance sensing at wound sites. *Sci. Adv.* **9**, eade4687 (2023).

42. Y. Ni, *et al.*, Photodegradable, Self-Healing, and Soft-Tough Transparent Elastomers Via Zinc Coordination for Transient Electronics. *Adv. Mater.* **38**, e07287 (2026).

43. M. Rüegg, R. Blum, G. Boero, J. Brugger, Biodegradable Frequency-Selective Magnesium Radio-Frequency Microresonators for Transient Biomedical Implants. *Adv. Funct. Mater.* **29**, 1903051 (2019).

44. H. Zhang, K. Zhang, J. A. Rogers, Y. Huang, An analytical model of reactive diffusion for transient electronics with thick encapsulation layer. *Mech. Mater.* **191**, 104954 (2024).

45. D. Zhang, S. Ma, J. Nachtsheim, S. Zhang, B. Markert, A variational phase-field framework for multiphysics modelling of degradation and stress corrosion cracking in biodegradable magnesium alloys. *J. Mech. Phys. Solids* **190**, 105694 (2024).

46. D. Gastaldi, *et al.*, Continuum damage model for bioresorbable magnesium alloy devices — Application to coronary stents. *J. Mech. Behav. Biomed. Mater.* **4**, 352–365 (2011).

47. K. van Gaalen, *et al.*, Linking the effect of localised pitting corrosion with mechanical integrity of a rare earth magnesium alloy for implant use. *Bioact. Mater.* **21**, 32–43 (2023).

48. K. van Gaalen, *et al.*, Predicting localised corrosion and mechanical performance of a PEO surface modified rare earth magnesium alloy for implant use through in-silico modelling. *Bioact. Mater.* **26**, 437–451 (2023).

49. C. Quinn, K. Van Gaalen, P. E. McHugh, A. Kopp, T. J. Vaughan, An enhanced phenomenological model to predict surface-based localised corrosion of magnesium alloys for medical use. *J. Mech. Behav. Biomed. Mater.* **138**, 105637 (2023).

50. E. L. Boland, C. J. Shine, N. Kelly, C. A. Sweeney, P. E. McHugh, A Review of Material Degradation Modelling for the Analysis and Design of Bioabsorbable Stents. *Ann. Biomed. Eng.* **44**, 341–356 (2016).

51. J. A. Rogers, T. Someya, Y. Huang, Materials and Mechanics for Stretchable Electronics. *Science* **327**, 1603–1607 (2010).

52. Q. Ma, *et al.*, A nonlinear mechanics model of bio-inspired hierarchical lattice materials consisting of horseshoe microstructures. *J. Mech. Phys. Solids* **90**, 179–202 (2016).

53. S.-W. Hwang, *et al.*, A Physically Transient Form of Silicon Electronics. *Science* **337**, 1640–1644 (2012).

54. Q. Lu, *et al.*, Degradation Mechanism and Control of Silk Fibroin. *Biomacromolecules* **12**, 1080–1086 (2011).

55. S.-K. Kang, *et al.*, Dissolution Behaviors and Applications of Silicon Oxides and Nitrides in Transient Electronics. *Adv. Funct. Mater.* **24**, 4427–4434 (2014).

56. F. von Burkersroda, L. Schedl, A. Göpferich, Why degradable polymers undergo surface erosion or bulk erosion. *Biomaterials* **23**, 4221–4231 (2002).

57. J. Gonzalez, R. Q. Hou, E. P. S. Nidadavolu, R. Willumeit-Römer, F. Feyerabend, Magnesium degradation under physiological conditions – Best practice. *Bioact. Mater.* **3**, 174–185 (2018).

58. B. Bourdin, Filters in topology optimization. *Int. J. Numer. Methods Eng.* **50**, 2143–2158 (2001).

59. T. E. Bruns, D. A. Tortorelli, Topology optimization of non-linear elastic structures and compliant mechanisms. *Comput. Methods Appl. Mech. Eng.* **190**, 3443–3459 (2001).

60. M. Park, *et al.*, Skin-integrated systems for power efficient, programmable thermal sensations across large body areas. *Proc. Natl. Acad. Sci.* **120**, e2217828120 (2023).

61. S. Jafarzadeh, Z. Chen, S. Li, F. Bobaru, A peridynamic mechano-chemical damage model for stress-assisted corrosion. *Electrochimica Acta* **323**, 134795 (2019).

62. C. Xie, S. Bai, X. Liu, M. Zhang, J. Du, Stress-corrosion coupled damage localization induced by secondary phases in bio-degradable Mg alloys: phase-field modeling. *J. Magnes. Alloys* **12**, 361–383 (2024).

63. N. Lu, C. Lu, S. Yang, J. Rogers, Highly Sensitive Skin-Mountable Strain Gauges Based Entirely on Elastomers. *Adv. Funct. Mater.* **22**, 4044–4050 (2012).

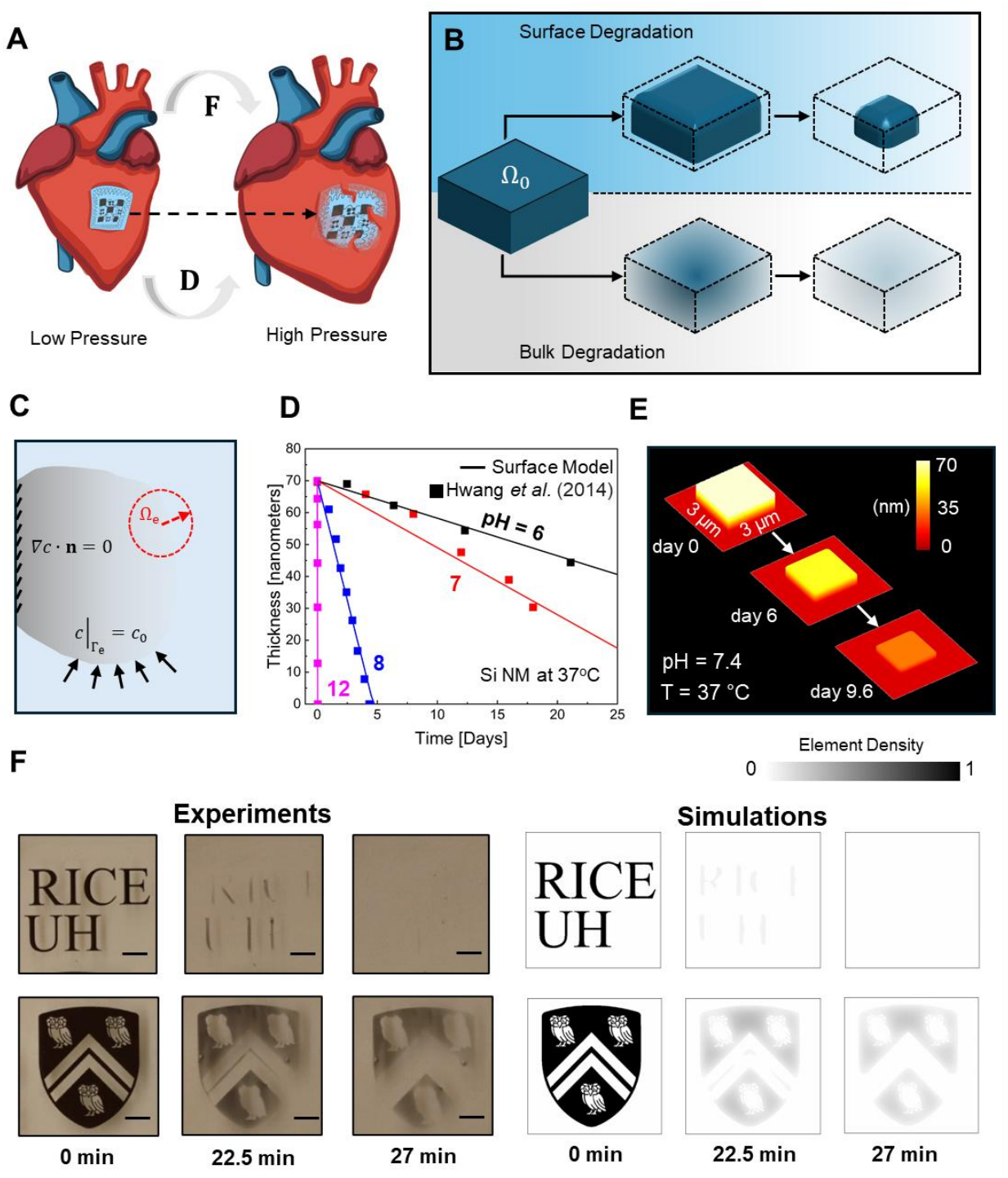

Fig. 1. Overview of Transient Degradation Modeling. (A) Schematic illustration of a bioresorbable electronic system in the epicardium undergoing coupled mechanical deformation and material degradation. **(B)** Conceptual distinction between surface-limited and bulk degradation mechanisms, highlighting their characteristic spatial profiles of material loss. **(C)** Density-based filtering approach used to model material degradation, with representative boundary conditions. **(D)** Simulated thickness reduction of a 70 nm silicon nanomembrane as a function of time and pH, compared with experimental measurements under surface-driven degradation. **(E)** Simulated thickness and lateral reduction of the 70 nm silicon nanomembrane. **(F)** Experimental and simulated degradation of a 100 nm magnesium film patterned with 'RICE,' 'UH,' and the Rice University shield (scale bar 5 mm).

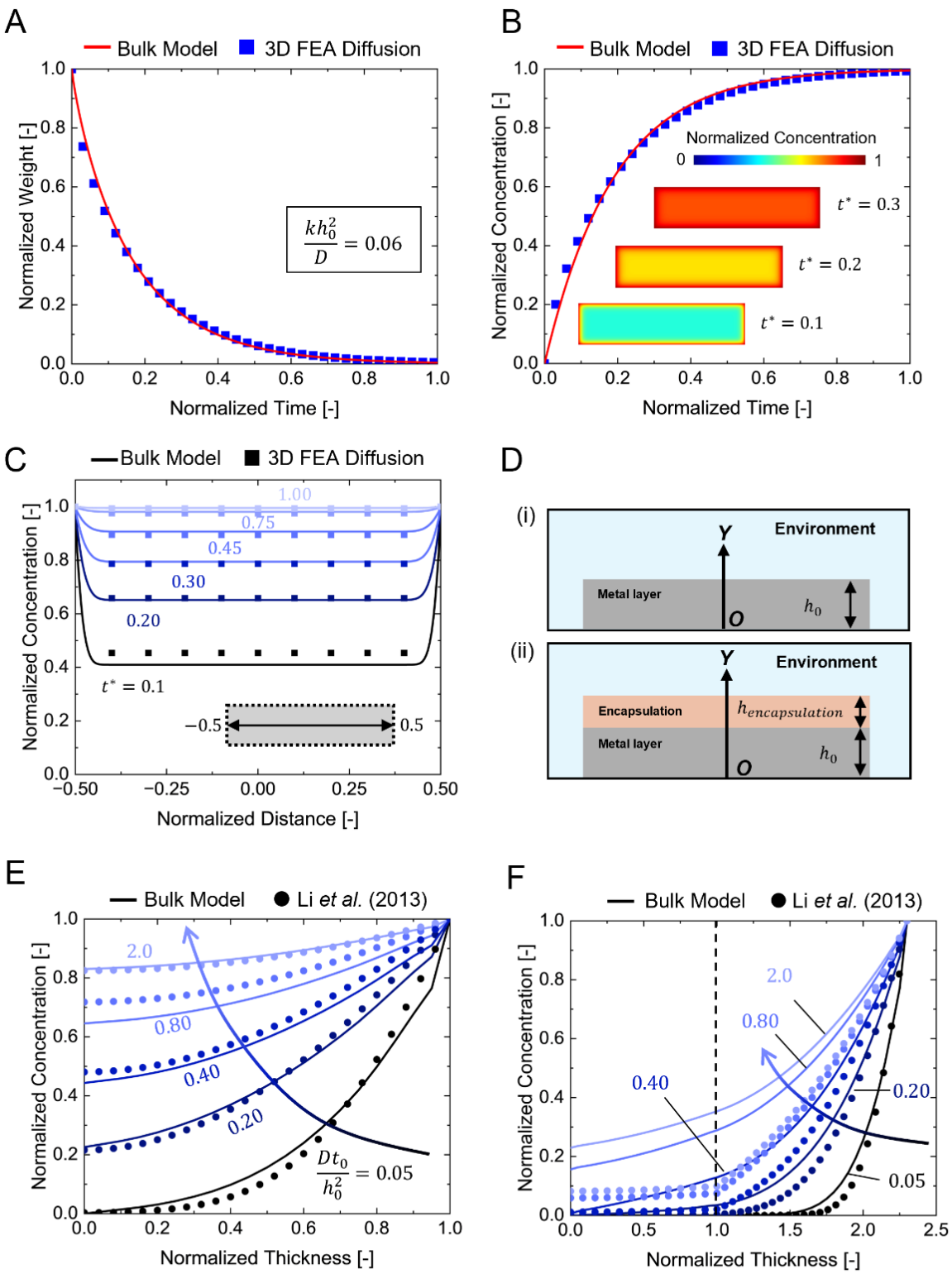

Fig. 2. Numerical and Analytical Benchmarking (A) Normalized weight change predicted by the bulk degradation model and the full three-dimensional diffusion model. **(B)** Temporal and spatial evolution of normalized water concentration at the centroid of a representative Mg sample. **(C)** Normalized water concentration profiles along the longitudinal direction of the Mg sample at selected non-dimensional times. **(D)** Schematic illustration of boundary conditions for (i) a single metal layer and (ii) an encapsulation–metal bilayer configuration. **(E–F)** Comparison between the bulk degradation model and one-dimensional analytical solutions for normalized water concentration: **(E)** in Mg and **(F)** in Mg/MgO.

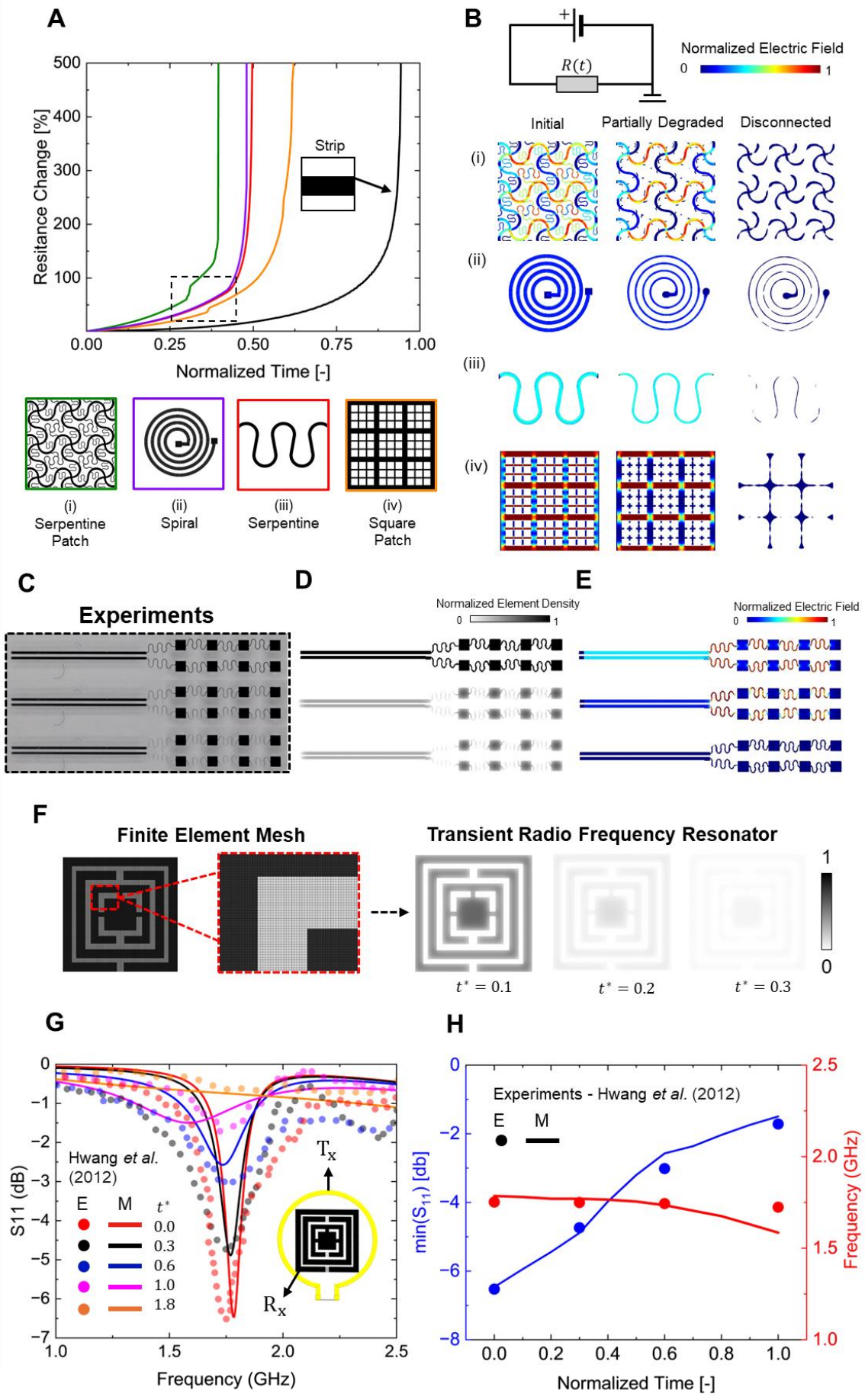
A
Resitance Change [%]
Normalized Time [-]
Strip
(i) Serpentine Patch
(ii) Spiral
(iii) Serpentine
(iv) Square Patch
B
R(t)
Normalized Electric Field
Initial
Partially Degraded
Disconnected
C
Experiments
D
Normalized Element Density
E
Normalized Electric Field
F
Finite Element Mesh
Transient Radio Frequency Resonator
t* = 0.1
t* = 0.2
t* = 0.3
G
S11 (dB)
Frequency (GHz)
Hwang et al. (2012)
E M t*
0.0
0.3
0.6
1.0
1.8
Tx
Rx
H
Experiments - Hwang et al. (2012)
min(S11) [db]
Frequency (GHz)
Normalized Time [-]

Fig. 3. Modeling Transient Degradation in Electronic Circuits. (A) Simulated temporal evolution of normalized electrical resistance during degradation for representative circuit geometries: (i) serpentine patch, (ii) spiral, (iii) single serpentine, and (iv) square patch. **(B)** Schematic illustration of electrical boundary conditions and electric field distributions at the initial, partially degraded, and electrically disconnected states. **(C–E)** Degradation of a neural probe design shown by **(C)** dissolution experiments, **(D)** simulated element density field, and **(E)** simulated normalized electric field distribution. **(F)** Finite element mesh of a metamaterial antenna resonator and the corresponding degraded configuration at representative nondimensional times. **(G)** Time-dependent reflection coefficient (S_{11}) of the antenna receiver under excitation from the transmitter coil (E: Experiments, M: Model). **(H)** Modeled evolution of the reflection coefficient (S_{11}) and resonant frequency during degradation (E: Experiments, M: Model).

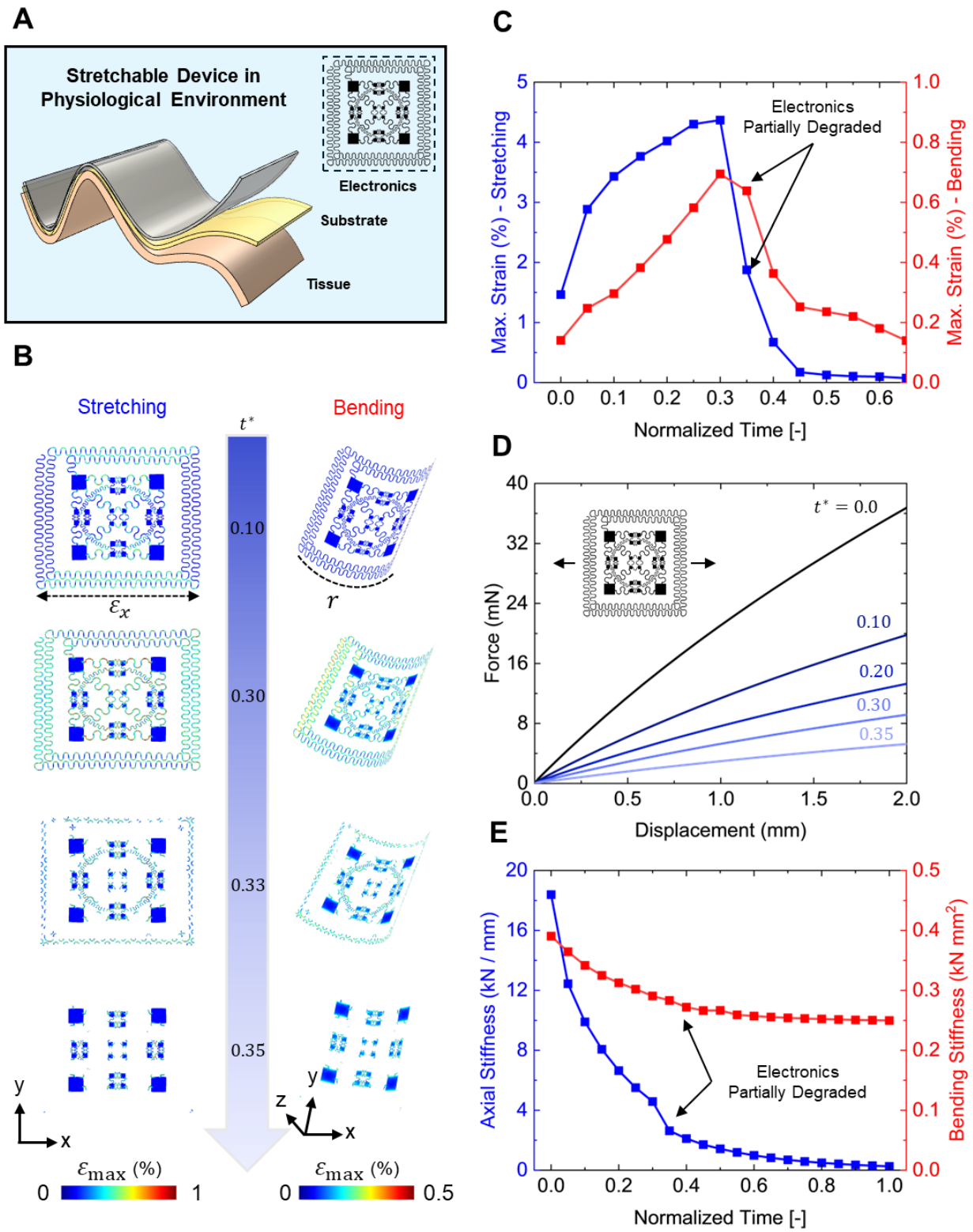

Fig. 4. Modeling Transient Degradation in Stretchable Circuits. (A) Schematic illustration of the material layout (tissue, substrate, and electronics) and geometric configuration of a canonical transient stretchable structure on soft tissue. **(B)** Simulated time-dependent distribution of maximum principal strain in the metal layer under 20% uniaxial stretching and bending with a radius of 3.75 mm at representative dissolution times, highlighting sequential circuit resorption. **(C)** Maximum principal strain in the metal layer as a function of normalized degradation time for the stretching and bending cases shown in **(B)**. **(D)** Time-dependent force–displacement response under axial stretching during degradation. **(E)** Simulated evolution of effective stretching and bending stiffness during degradation, indicating the onset of partial degradation and saturation at longer resorption times.

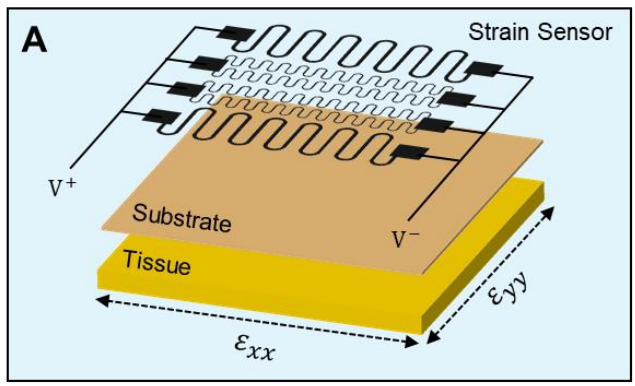

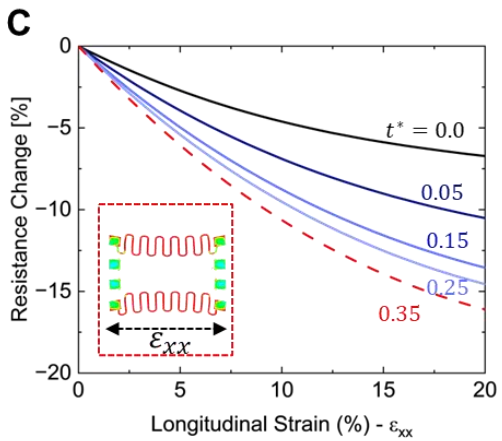

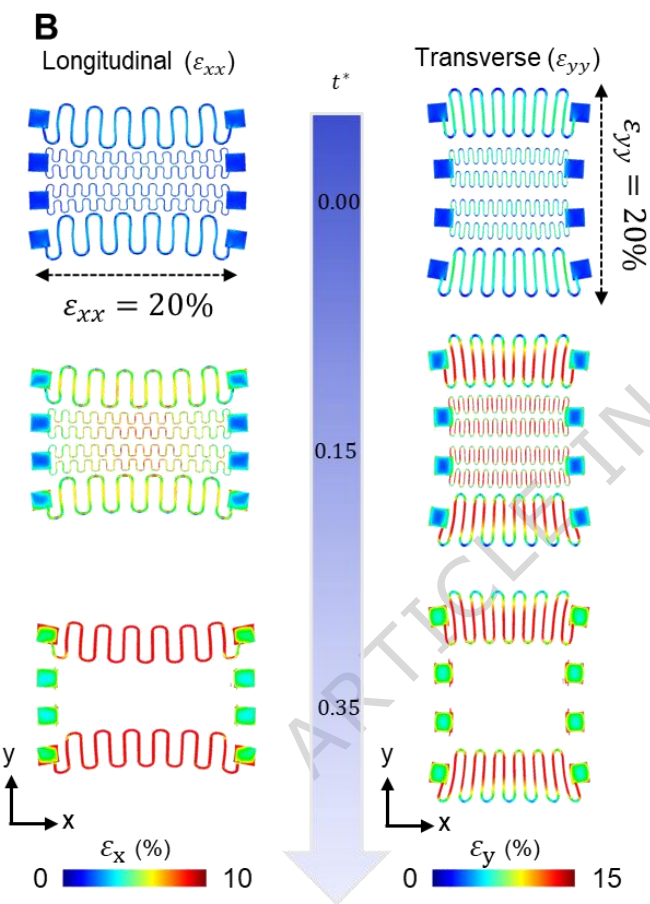

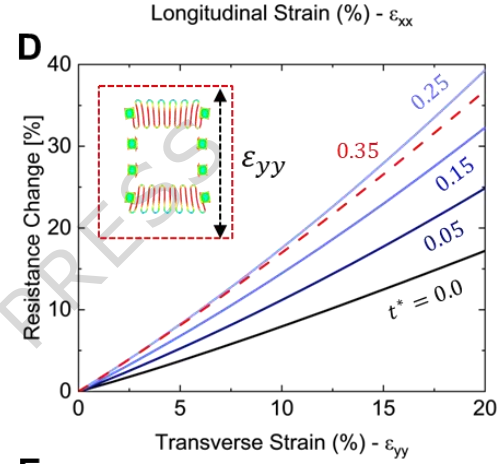

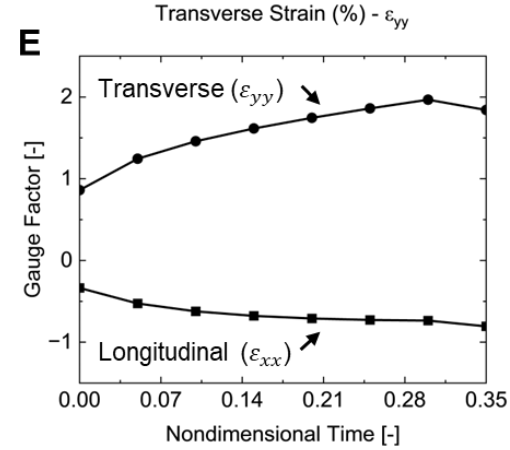

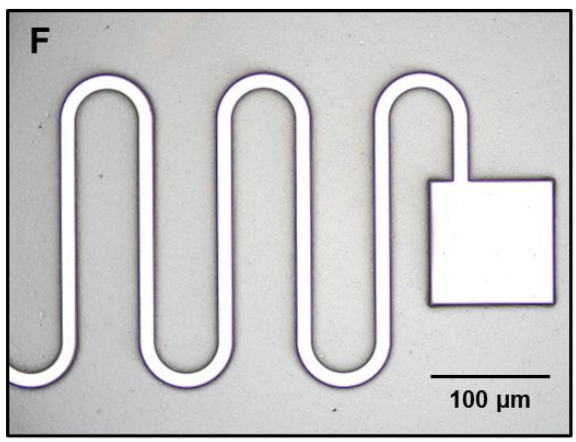

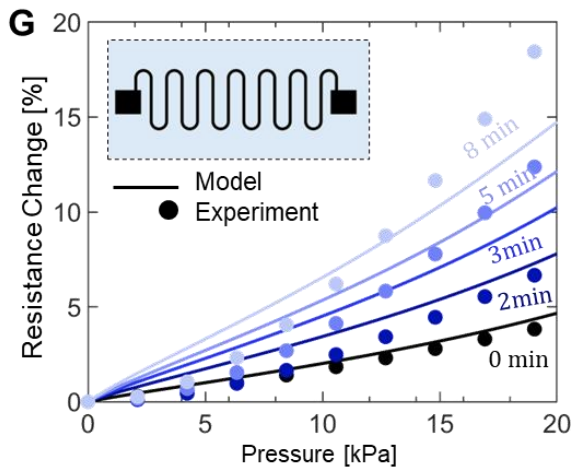

Fig. 5. Modeling Validation in Transient Stretchable Strain Sensor. (A) Schematic illustration of a stretchable strain sensor mounted on a substrate and soft tissue, with corresponding electrical boundary conditions, and subjected to longitudinal and transverse strain. **(B)** Simulated strain distributions under 20% stretching along the longitudinal and transverse directions at representative nondimensional times, highlighting circuit dissolution. **(C–D)** Time-dependent nonlinear resistance change as a function of applied strain, up to 20%, along **(C)** the longitudinal direction and **(D)** the transverse direction. **(E)** Sensitivity (gauge factor) of the stretchable strain sensor as a function of normalized time for longitudinal and transverse strain. (**F**) Optical image of stretchable strain sensor. (**G**) Experimental and simulated pressure-dependent relative resistance changes of the stretchable bioresorbable sensor at different stages of dissolution (0–8 min).

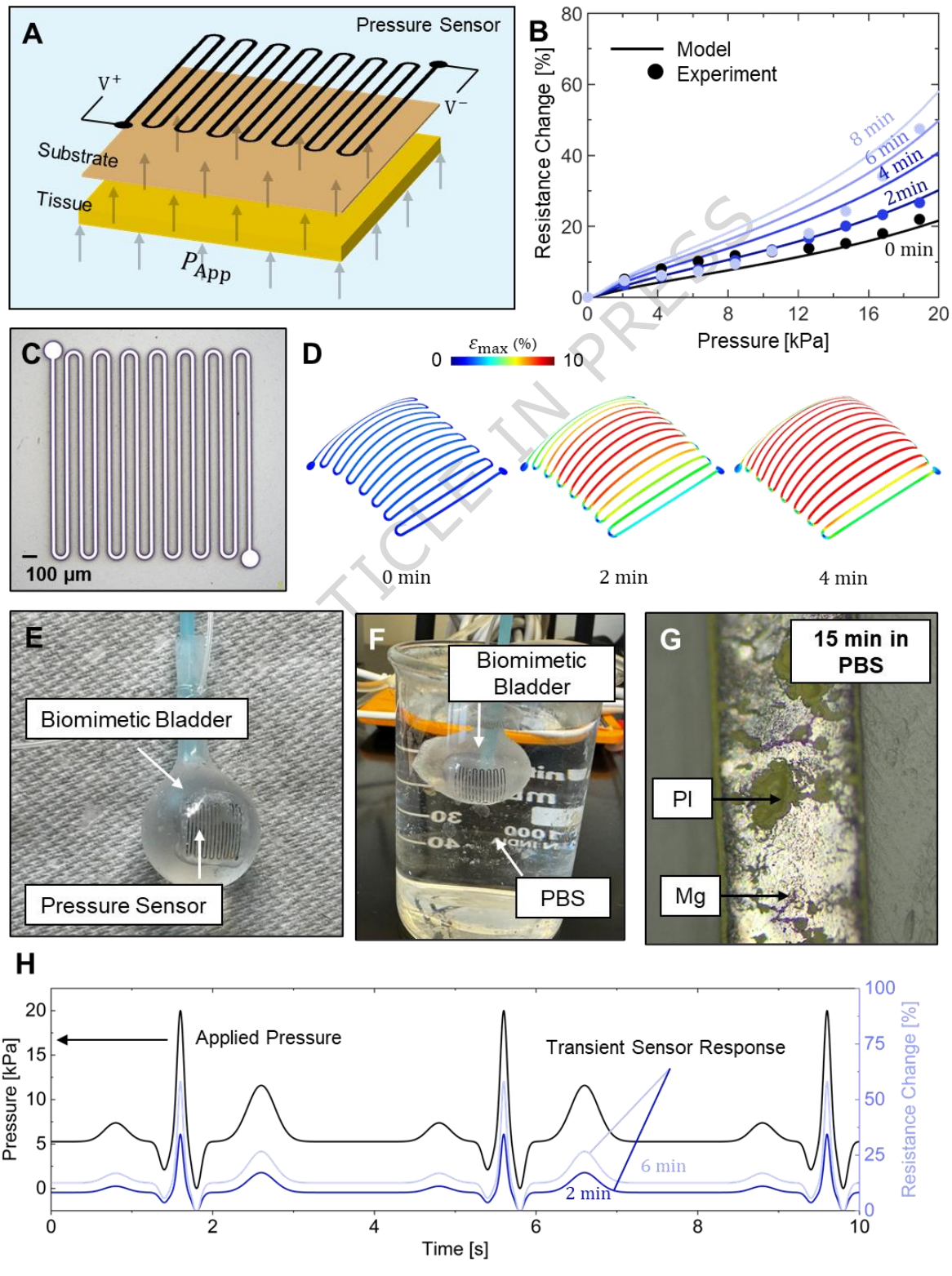

Fig. 6. Modeling Validation in Transient Stretchable Pressure Sensor. (A) Schematic illustration of a stretchable pressure sensor mounted on a substrate and soft tissue and subjected to applied pressure. **(B)** Experimental and simulated nonlinear time-dependent resistance change as a function of applied pressure, with increasing sensitivity as degradation progresses. (**C**) Optical image of the fabricated pressure sensor. (**D**) Finite element simulations showing the corresponding strain distributions at 0 min, 2 min, and 4 min. **(E)** bioresorbable pressure sensor mounted on the surface of a biomimetic bladder. (**F**) Sensor–bladder assembly immersed in PBS to initiate resorption. (**G**) Optical image of the sensor after 15 min submersion in PBS, illustrating the non-uniform degradation profile of the Mg conductive traces. **(H)** Transient response of the pressure sensor to a prescribed electrocardiogram-like pressure waveform, demonstrating the ability of the sensor to reproduce time-dependent resistance changes during degradation.

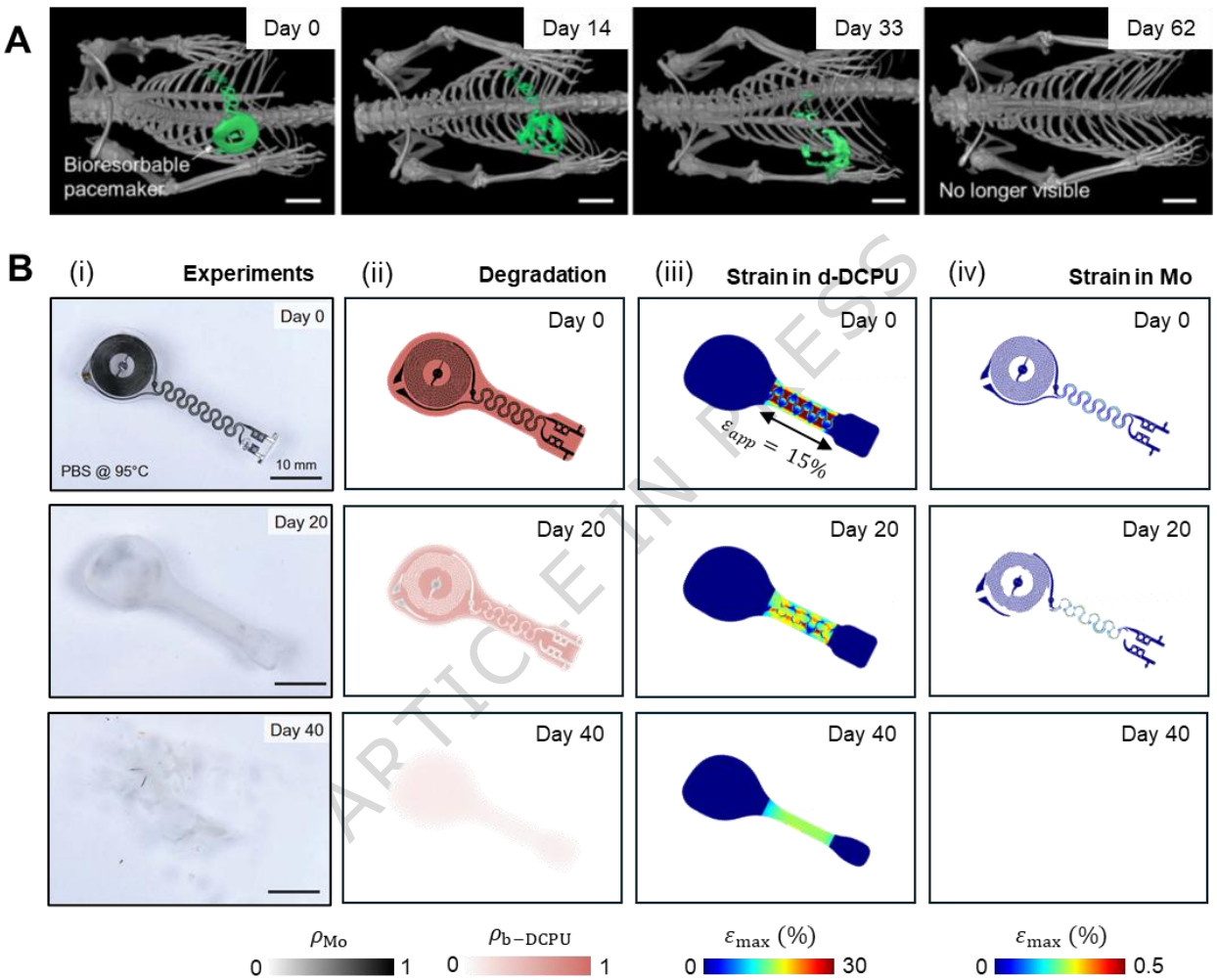

Fig. 7. System-Level Modeling in Bioresorbable Pacemaker. (A) Three-dimensional computed tomography (CT) images of rats collected over 9 weeks after implantation of a bioresorbable device. Reproduced with permission from the American Association for the Advancement of Science from (6). (B) System-level simulations at day 0, day 20, and day 40. (i) Optical micrographs showing progressive physical dissolution of the device in PBS at 95 °C at different degradation stages. (ii) Simulated evolution of substrate degradation, represented by the density field $\rho_{\text{b-DCPU}}$ and ρ_{Mo}. (iii) Simulated strain distributions in the biodegradable substrate (b-DCPU) under an applied strain of $\varepsilon_{\text{app}} = 15\%$. (iii) Simulated strain distributions in the Mo interconnects during degradation.

Table 1. Representative bioresorbable electronic systems and their classification into one-way and two-way coupling regimes.

Device	Function	Conductive Material	Substrate / Encapsulation	Size	Deformation Mode	Local Strain	Coupling
Transient, closed-loop pacemaker system (5)	Temporary post-operative cardiac pacing	Mo, Si NM	PLGA, b-DCPU	~10 × 30 × 0.35 mm³	Tensile stretching (~10–20%)	<0.6%	One-way
Microelectromechanical systems (35)	Capacitive sensing, electrostatic actuation, and temporary diagnostics	Si NM, Mo, SiO_2	PAP	~1 × 1 × 0.1 mm³	Bending (R = 5–40 mm)	<1%	One-way
Millimeter-scale optoelectronic system (20)	Electrotherapy, temporary cardiac pacing.	Mg, Zn, MoO_3, Si	PLGA, Polyanhydride	~1.8 × 3.5 × 1.0 mm³	Mechanically decoupled	–	One-way
Temporary cardiac pacemaker (6)	Temporary post-operative cardiac pacing	W, Mg, Mo, Si NM	PLGA	~10 × 30 × 0.35 mm³	Conformal compression (20%), Bending (R ~5 mm), Twisting angle (180°)	<0.6%	One-way
Ultrasound neurostimulator (11)	Electrotherapy, temporary nerve stimulation	Mg	PHBV	~10 × 10 × 0.03 mm³	Bending (R ~0.5 mm)	<0.6%	One-way
Compliant cardiac patch (7)	Promote growth of cardiac cells	Mo	POCO, PEG-LA-DA	~30 × 30 × 0.135 mm³	Tensile strain (50–100%)	<0.6%	Two-way
Thermo-responsive surgical electronic mesh (16)	Hernia repair and pressure monitoring	Mg	PLCL	~25 mm radius × 0.36 mm	Inflatable (30 kPa), bending and stretching	1–3%	Two-way
Neural electrode arrays (36)	Multiplex neural sensing	Si NM, SiO_2	PLGA	~30 × 35 × 0.033 mm³	Bending (R ~1 mm)	<0.05%	One-way
Soft, organic electrodes (37)	Neural stimulation	ETE-S / ETE-PC	PEDOT-S	~30 × 50 × 100 μm³	Mechanically decoupled	–	One-way
Passive pH sensor (27)	Gastric leakage monitoring	Zn	PDPAEMA-PEGDA	~12 mm radius × 0.6 mm	Volumetric expansion	>0.6%	Two-way
Stretchable strain and pressure sensor (25)	Orthopaedic rehabilitation monitoring	Mg	POMaC, PGS, PLLA	~20 × 10 × 1.5 mm³	Tensile strain (~15%), Pressure (80 kPa)	>2%	Two-way
Crack-based strain sensor (38)	Vascular surface strain monitoring	W, Mo, Mg. MoO_3	PCL	~20 mm × 0.2 mm × 50 nm	Tensile strain (~10%)	~1.5%	Two-way
Neural interface for pain management (39)	Neuropathic pain block	Au, Mo	PA, Silk	~30 × 10 × 0.25 mm³	Tensile strain (~20%),Bending (R ~1.5 mm), Twisting angle (45°)	<0.2%	Two-way
Dual neural stimulator (40)	Peripheral nerve regeneration	Mo	PA, PLGA, PU	~20 × 5 × 0.35 mm³	Tensile strain (~19%)	~0.6%	Two-way
Electrotherapy system (41)	Wound healing and impedance sensing	Mo, MoO_3	Freestanding in wound	~2.5 × 5 × 0.25 mm³	Biaxial strain (7%), Tensile strain (~9%), Bending (R ~4.0 mm), Twisting angle (60°)	~0.3%	One-way
Flexible and transparent keyboard (42)	Human–machine interfaces	EGaIn	Zn-MDPU	~20 × 10 × 0.1 mm³	Tensile strain (~500%)	~100%	Two-way
Wireless microheaters (43)	Power transfer in implants	Mg	Glass	~1.28 mm radius × 2 μm	Mechanically decoupled, Thermal trigger	–	One-way
Electrochemical drug delivery platform (14)	Programmable drug release	Mg, SiO_2, Si NM	PLGA, PBTPA	~20 × 20 × 5 mm³	Mechanically decoupled	–	One-way